

AD-A099 640

CALIFORNIA UNIV SANTA BARBARA QUANTUM INST

F/6 7/4

TUNNELING SPECTROSCOPY FOR THE STUDY OF ADSORPTION AND REACTION—ETC(U)

MAY 81 R M KROEKER, P K HANSMA

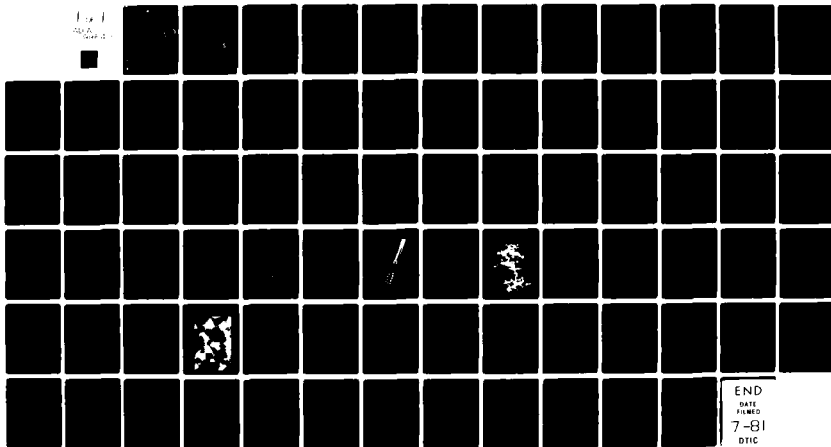
N00014-78-C-0011

NL

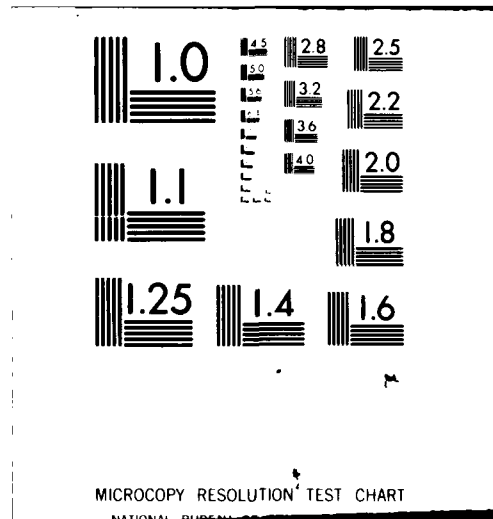
UNCLASSIFIED

TR-8

100-1  
100-1



END  
DATE  
FILMED  
7-81  
DTIC



AD A099640

LEVEL II

12

OFFICE OF NAVAL RESEARCH  
Contract N0014-78-C-0011

Task No. NR056-673

Technical Report

9

Tunneling Spectroscopy for the Study of  
Adsorption and Reaction on Model Catalysts.

by

R. M. Kroeker and P. K. Hansma

18 N0014-78-C-0011

Prepared for Publication  
in  
Catalysis Review

IBM San Jose Research Laboratory (RMK)  
San Jose, CA  
Department of Physics (PKH)  
Quantum Institute -  
University of California  
Santa Barbara, CA

1981

27 May 81

DTIC  
ELECTE  
JUN 2 1981

12 79

Reproduction in whole or in part is permitted for  
any purpose by the United States Government.

This document has been approved for public release  
and sale; its distribution is unlimited.

DTIC FILE COPY

4

81 6 01 091

REPORT DOCUMENTATION PAGE		READ INSTRUCTIONS BEFORE COMPLETING FORM
1. REPORT NUMBER	2. GOVT ACCESSION NO. <b>AD-A099640</b>	3. RECIPIENT'S CATALOG NUMBER
4. TITLE (and Subtitle) Tunneling Spectroscopy for the Study of Adsorption and Reaction on Model Catalysts.		5. TYPE OF REPORT & PERIOD COVERED Technical Report
7. AUTHOR(s) R. M. Kroeker and P. K. Hansma		6. PERFORMING ORG. REPORT NUMBER
9. PERFORMING ORGANIZATION NAME AND ADDRESS Quantum Institute, Physics Dept. Univ. of California, Santa Barbara, CA 93106		8. CONTRACT OR GRANT NUMBER(s) N0014-78-C-0011✓
11. CONTROLLING OFFICE NAME AND ADDRESS Office of Naval Research Department of the Navy Arlington, VA 22217		10. PROGRAM ELEMENT, PROJECT, TASK AREA & WORK UNIT NUMBERS NRO56-6731
14. MONITORING AGENCY NAME & ADDRESS (if different from Controlling Office)		12. REPORT DATE May 27, 1981
		13. NUMBER OF PAGES 58
		15. SECURITY CLASS. (of this report) Unclassified
		15a. DECLASSIFICATION/DOWNGRADING SCHEDULE
16. DISTRIBUTION STATEMENT (of this Report) Approved for public release and sale; distribution unlimited.		
17. DISTRIBUTION STATEMENT (of the abstract entered in Block 20, if different from Report)		
18. SUPPLEMENTARY NOTES		
19. KEY WORDS (Continue on reverse side if necessary and identify by block number) Tunneling Spectroscopy, Model Catalysts, Rhodium, Iron, Nickel, Aluminum Oxide, Adsorbed Carbon Monoxide, Identification of Surface Species, Vibrational Spectroscopy, Vibrational mode Shifts. <i>ganina</i>		
20. ABSTRACT (Continue on reverse side if necessary and identify by block number) Inelastic Tunneling Spectroscopy has been used to study model catalyst systems. Model systems include oxidized alumina as a model for <i>γ</i> -alumina and oxidized magnesium as a model for magnesia. Evaporated metals serve as models for supported metal catalysts. Detailed studies include CO adsorption and hydrogenation on rhodium, sulfur poisoning and the effect of top metal electrodes on the spectra. <i>4</i>		

Tunneling Spectroscopy for the Study of  
Adsorption and Reaction on Model Catalysts

R.M.Kroeker  
IBM San Jose Research Laboratory  
5600 Cottle Road  
San Jose , CA 95193

and

P.K.Hansma  
Department of Physics  
University of California  
Santa Barbara , CA 93106

I. INTRODUCTION

Inelastic electron tunneling spectroscopy measures the vibrational modes of a small quantity of molecules that are included in or near the insulating layer of a metal-insulator-metal tunnel junction (1,2). Figure 1 shows two metal electrodes separated by a thin insulating layer. If this layer is thin enough (of order 20 Angstroms) and if a voltage  $V$  is applied between the two electrodes, an electron current will flow from one electrode to the other. The maximum energy of the tunneling electrons will be of order  $eV$ . If there is a molecule in or near the insulating layer with a characteristic vibrational mode energy  $h\nu$ , this vibrational mode may or may not be excited by the tunneling electron. The most important factor turns out to be simply, does the tunneling electron have enough energy? In particular, is  $eV \geq h\nu$ ?

Thus, inelastic electron tunneling in which the electron excites the molecular vibration will have a threshold at a voltage  $V=h\nu/e$ . At this threshold voltage, there will be a slight increase in the conductance of the tunnel junction due to the opening of the inelastic tunneling channel.

This slight increase in the conductance is generally observed experimentally as a peak in the second derivative as shown in the idealized spectra of Fig. 1.

The bottom of Fig. 1 shows the actual situation. The metal-insulator-metal junctions of the idealized view are formed at the intersections of evaporated aluminum and lead strips. The insulating layer is formed by the oxidation of the aluminum strip. The actual tunneling spectra shows a number of peaks because there are a number of vibrational modes for the molecule benzoic acid used for this sample.

The spectral range of tunneling spectroscopy includes all molecular vibrations. The range from 50 meV ( $\approx 400 \text{ cm}^{-1}$ ) to beyond the energy of molecular vibrations (beyond 500 meV,  $\approx 4000 \text{ cm}^{-1}$ ) requires no special care. The range below 50 meV contains strong metal phonon bands in addition to molecular vibrations. These phonon bands, which can interfere with the observation of molecular vibrations, can be minimized with differential tunneling spectroscopy (3). The traces in Fig. 2 are differential tunneling spectra: the difference spectra between a doped and an undoped junction. Note that the spectral range extends down to 0 meV.

Since the theory of tunneling spectroscopy has been reviewed elsewhere (4-10), here we will merely state that the dominant interaction between the tunneling electrons and the molecule is currently believed to be the long-range Coulomb interaction between the electron and the charge distribution of the molecule. Since a charged electron interacts much more strongly with a molecule than a chargeless photon of electromagnetic

radiation, tunneling spectroscopy is intrinsically more sensitive than infrared or Raman spectroscopy. Its sensitivity is roughly 1/100 of a monolayer over the area of a tunnel junction, which can be as small as 100×100 microns (11).

The resolution of tunneling spectroscopy depends upon the temperature and the modulation voltage used for obtaining the second derivative that is plotted on the y-axis. Table 1 shows the resolution for two representative temperatures and three modulation voltages. Note that

the resolution varies roughly over the range of 10 to 30 cm<sup>-1</sup>. The world record for resolution, set by Walmsley and co-workers, is less than 2 cm<sup>-1</sup> obtained with a small modulation voltage in a helium dilution refrigerator (12). These high resolutions are not commonly used, however, because the relative trace time, that is, the time to obtain a spectrum with the same signal to noise, rises rapidly as the resolution improves. Thus most spectra are taken at the poorest resolution sufficient to obtain the information desired. The table also includes the small upshifts in peak positions caused by a superconducting lead electrode (13).

There are basically no selection rules in tunneling spectroscopy: in general, all the vibrations of a molecule can be observed. Work in several laboratories has shown that both infrared and Raman active modes are present with comparable intensities (14,15). The point is that the source of optical selection rules, which is the uniformity of the electric field due to the electromagnetic radiation over the size of a molecule, is not present in tunneling spectroscopy. The electric field of an electrode passing through the insulating layer varies considerably on the scale of molecular dimensions.

Accession for	
NTIS GRAM	
DTIC TAB	
Unannounced	
Justification	
By	
Distribution/	
Availability Codes	
Avail and/or	
Special	
A	

There is a selection preference for modes that oscillate perpendicular to the plane of the tunneling barrier. For example, in Fig. 3, the modes with subscripts s, for symmetric, involve vibrations of the methane sulfonate ion perpendicular to the plane of the insulator while the modes with subscripts a, for antisymmetric, involve oscillation parallel to the plane. There is a slight preference for the perpendicular modes. It is clear, however, that this is not a selection rule, merely a selection preference (16).

Finally, there appears to be a relatively strong selection preference against optically inactive modes. These modes, which are neither infrared nor Raman active, occur for a few highly symmetric molecules (e.g., the  $A_{1g}$  modes of anthracene). Kirtley et al. found these modes to be between one and two orders of magnitude weaker than the optically active modes in their tunneling spectra (17). These selection preferences are understandable within the framework of the transfer Hamiltonian theory of tunneling spectroscopy. More detailed information on theory, sensitivity, selection rules, orientational effects, and spectral range can be obtained in review articles (4-10) as well as the above references.

## II. PROBLEMS WITH TUNNELING SPECTROSCOPY FOR THE STUDY OF CATALYSIS

### A. Peak Shifts Due to the Top Metal Electrodes

It is, of course, surprising that vibrational spectra can be obtained at all using tunneling spectroscopy. Why doesn't the top metal electrode completely destroy the molecules on top of which it has evaporated? In fact, many evaporated metals such as gold, chromium, and aluminum seem to do precisely that. Despite repeated attempts, we have rarely succeeded in



getting good vibrational spectra with these metals as top electrodes. Fortunately, other metals, in particular; lead (our all-around favorite), thallium, and under some circumstances, indium, tin, and silver all can be evaporated without destroying the layer of molecules.

Even if the layer of molecules is not destroyed, aren't the vibrational modes strongly perturbed by the top metal electrode? This is a question that can be answered by experiment. Among the first experiments was by Kirtley, et al., on the effect of the top metal electrodes on mode positions of the benzoate ions and hydroxyl ions absorbed on alumina (13). He found that the position of the hydroxyl group stretching mode moved around by a few percent from metal electrode to metal electrode, while the vibrational modes of the benzoate ions moved typically less than a percent. Figure 4 summarizes his findings and recent estimates for the peak shifts of CO stretching vibrations. A number of other experiments have been done simply comparing vibrational mode positions with the top metal electrode to those measured optically without a top metal electrode; a representative experiment is that by McMorris, et al. (18). No peak shift of greater than a few percent has even been recorded, to our knowledge, for any triatomic or larger molecule. Most of the shifts have been unobservable within experimental accuracy of the measurements (of order tenths of a percent).

At this point, it seems safe to conclude that the vibrational modes of reasonably large molecules are not significantly perturbed by the top metal electrodes. Very small molecules such as OH and CO are significantly perturbed. Recent experiments by Bayman et al. (19) have shown dramatic changes in the spectra of CO absorbed on iron particles on alumina as

shown in Fig. 5. Hipps and Mazur (20) have shown significant changes in the spectra of the complex  $\text{KFe(CN)}_6$  for Pb, Ag, and Sn top metal electrodes. They concluded that Pb had the least tendency toward chemical interaction with the complex.

These dependences on top metal electrodes must, however, serve to caution us about the reliability of tunneling measurements as a measure of the unperturbed vibrational frequencies for CO on model supported metal catalysts and for model cluster catalysts.

#### B. Cryogenic Temperatures

A second problem with tunneling spectroscopy is that cryogenic temperatures must be used to measure the spectra. While this is certainly a day-to-day nuisance, it is not as significant as might first be believed. In particular, the resolution required for most work can be obtained at 4.2K. For this temperature, it is unnecessary to transfer or handle liquid helium except to receive it from the vendor and return the used dewars roughly a month later. For the month, the samples can be simply slipped down the neck of the vendor's storage dewar, using probes similar to the one shown in Fig. 6.

A more fundamental problem is that tunneling spectra cannot be run at actual reaction conditions. This is a serious problem which cannot be overcome at present. The most that can be done is to chill the sample rapidly from reaction conditions and see what is on the surface.

#### C. Experimental Constraints on the Sample Thickness

What catalysts can be studied with inelastic electron tunneling spectroscopy? One answer to this question is none. No actual catalyst has

been studied by tunneling spectroscopy. It has not yet been possible to take an industrial catalyst sample and characterize it with tunneling spectroscopy. Figure 7 shows again the geometry of the tunnel junction. The point is that unknowns can be placed in the region marked with question marks. The catch is that the unknown layer must be thin enough for the electrons to tunnel through. That is, the unknown layer must either be considerably thinner than 100 Angstroms or an incomplete layer. It is not, at present, practical to put samples of commercial catalysts into this geometry. What can be done is the simulation of the essential features of commercial catalysts in model catalyst systems.

### III. MODEL SYSTEMS THAT CAN BE STUDIED WITH TUNNELING SPECTROSCOPY

#### A. Oxidized Alumina

To date the primary model system that has been studied is the oxidized aluminum itself. Does this oxidized aluminum resemble aluminas used as catalysts and catalyst supports? Figure 8 shows small balls of aluminum produced by evaporating aluminum in an inert atmosphere. When these balls are oxidized in air, they form a relatively large surface area of oxidized aluminum. Nitrogen BET measurements gave 13.6 meters<sup>2</sup> per gram in agreement with the average radius of order 800 Angstroms. This type of sample provided enough surface area for conventional catalyst evaluation techniques. Thermogravimetric analysis and butene isomerization reactions showed this catalyst to be not significantly hydrated and similar in catalytic activity to standard  $\gamma$ -alumina catalysts (21). Vibrational spectra are in agreement with this conclusion (22). That is, no species have been found with tunneling spectroscopy adsorbed on oxidized aluminum that are inconsistent with species found by optical spectroscopy adsorbed

on  $\gamma$ -alumina. A large number of species have been studied (4-10,16,23-28).

Two groups have studied hydrogenation by the hydroxylated alumina surface. Figure 9 shows Jaklevic's results for the hydrogenation of propiolic acid (29) and Fig. 10 shows Hall and McBride's result for hydrogenation of a dicarboxylic acid (30). In each case, it was believed that the hydroxyl groups on the surface served as the source of the hydrogen. It is not at present clear whether these reactions could be run catalytically using water or some other source of hydrogen to replenish the hydroxyl groups on the surface.

Evans and Weinberg have done detailed measurements on the adsorption of ethanol, acetaldehyde and acetic acid on alumina (31). All of these compounds could, under suitable conditions, be made to produce acetate ions on the alumina surface. The subtle differences between the resultant acetate ions were explored. This work complements the infrared studies on catalytic dehydration of alcohol and the conversion of alcohols to aldehydes and the condensation reactions of aldehydes.

Recently Walmsley and co-workers have obtained the spectra of unsaturated hydrocarbons on alumina (32). This may be useful in understanding important hydrogenation and polymerization reactions. Figure 11 shows a representative spectrum.

The tunneling barrier parameters have been determined by a number of groups by fitting the current-voltage curves to trapezoidal model calculations (20,33-37).

#### B. Oxidized Magnesium

Figure 12 shows recent work of Walmsley and co-workers for formic

acid adsorbed on oxidized aluminum and magnesium (38). They interpret shifts in positions of the symmetric  $\text{CO}_2$  modes of carboxylate ions to indicate stronger electrostatic bonding to surface magnesium cations than to surface aluminum cations. They commented that this is consistent with the usual identification of magnesium oxide as being a more basic oxide than aluminum oxide.

Figure 13 shows a representative spectrum from the many obtained for larger molecules on oxidized magnesium by Coleman and co-workers (39). The differences between spectra obtained on oxidized magnesium and aluminum were related to changes in the surface adsorption mechanism. They observed, for example, a softening of the aromatic C-H stretching mode corresponding to frequency downshifts of  $\approx 150 \text{ cm}^{-1}$  that suggested  $\pi$ -complex formation with surface-active sites for some compounds. This complex formation was accompanied by a dramatic depression of the ring-mode intensities relative to the intensities obtained when the bonding was ionic (e.g., after proton donation to the surface of an acidic proton).

### C. Supported Cluster Catalysts on Alumina

Though alumina has application as a catalyst, it is more widespread as a catalyst support. Three groups have applied tunneling spectroscopy to the study of supported catalysts on alumina. Figure 14 shows representative results from the study of Evans and Weinberg for the supported complex zirconium tetraborohydride (40,41,42,43). These samples were formed by exposing the alumina to the vapor of zirconium tetrahydride at a pressure of  $5 \times 10^{-2}$  torr for 15 minutes. The resultant surface complex was characterized with tunneling spectroscopy and then studied in its

interactions with  $\text{H}_2\text{O}$ ,  $\text{D}_2\text{O}$  and hydrocarbons. Perhaps the most interesting feature of the research, in addition to the demonstration that supported complexes can be studied by tunneling spectroscopy, was their observation of evidence for polymerization of acetylene on the model catalysts.

Hipps, Mazur, and Pearce (20,44) have studied  $\text{Fe}(\text{}^{12}\text{C}^{15}\text{N})_6^{4-}$  and  $\text{Fe}(\text{}^{12}\text{C}^{14}\text{N})_6^{4-}$  adsorbed on oxidized aluminum from dilute  $\text{H}_2^{16}\text{O}$  and 50%  $\text{H}_2^{18}\text{O}$  solutions. Their comparisons to infrared and Raman spectra of  $\text{K}_4\text{Fe}(\text{CN})_6$  salt, observed CN stretching frequencies and isotopic shifts enabled them to argue that the iron remains in the divalent state after adsorption.

More recently, Bowser and Weinberg have looked at chlorodicarbonyl rhodium dimer,  $[\text{RhCl}(\text{CO})_2]_2$ , on alumina (45). The bond of the complex to the alumina was determined to be a Rh-O bond formed after the cluster lost Cl through HCl liberation. This type of work will help in the understanding of this general type of "molecularly engineered" catalyst. The promise is higher selectivity due to well-defined surface structures.

#### D. Supported Metal Particle Catalysts on Alumina and Magnesia

Figure 15 shows the results of Evans et al. for the adsorption of ethanol on silver clusters supported on alumina (46). They form the silver clusters by evaporating silver metal onto the surface of the oxidized aluminum. Transmission electron microscopy showed that the silver was in the form of particles with an average size between 10 and 80 Angstroms. They found subtle differences between the resultant adsorbed species on silver particles vs. the adsorbed species on the support. These subtle differences could be observed because of the good resolution of tunneling

spectroscopy.

A schematic view of model supported metal catalysts is shown in Fig. 16. The metal to be supported is evaporated with a low average thickness onto the oxidized alumina. The thickness of the evaporated metal can be conveniently monitored with an oscillating quartz crystal. These commercially available devices can, without special modification, measure an average mass thickness of less than 1 Angstrom. Figure 17 shows a transmission electron microscope picture of such a catalyst. The large grains are grains of the aluminum in the aluminum metal electrodes. The catalyst particles are these small dots that speckle the picture. In this particular case, the average thickness was 4 Angstroms. The layer agglomerated into particles with diameters of order 20 Angstroms. Note the good dispersion and relative uniformity of particle size, making this a good model system.

In general, the supported transition metals, which have included rhodium, iron, cobalt, nickel, palladium, and platinum in our group, are evaporated from pure material wound on tungsten filaments. Does tungsten get into the evaporated deposits? This question can be addressed by Auger spectroscopy. Figure 18 shows the recent results of Dubois et al. showing that rhodium is deposited without resolvable tungsten contamination (47). Similar preliminary experiments on platinum and iron showed no tungsten contamination.

Figure 19 shows the results of J. Klein, et al., for CO adsorbed on such a Rh/alumina model catalyst (48). Note that two isotopes have been used to identify vibrational modes by their peak shifts. This is an

invaluable technique since, as discussed later in this review (and in reference 54), it can be used to distinguish vibrational modes that appear in the same frequency range (e.g., CO bending, M-(CO) stretching, M-C stretching, and M-O stretching).

Figure 20 shows the results of the same French group for CO adsorbed on a Rh/magnesia model catalyst (49). This illustrates that tunneling spectroscopy has the potential for examining the metal-support interactions that can have dramatic effects on product distributions for actual catalysts.

Figure 21 is a differential tunneling spectrum for CO on a Rh/alumina model catalyst (50). A differential tunneling spectrum measures the difference spectra between two junctions. In this case, it is the difference between two adjacent junctions, one with rhodium metal and one without. The small peak at roughly 0.12 electron volts is due to a cancellation error of the relatively large peak due to the aluminum oxide vibrations. The peak between 0.4 and 0.5 volts is due to OH groups that are present on both the support and the particles. The other peaks in this spectrum are all due to the CO on rhodium. There are two resolved peaks in the CO stretching region and three resolved peaks in the 400-800  $\text{cm}^{-1}$  region that contains metal-carbon stretching and bending vibrations. Figure 22 shows spectra made in a variety of conditions. These illustrate that the peaks in the previous spectra are not due to merely one species but, in fact, three species.

Three species have been observed with infrared spectroscopy and ascribed to a gem dicarbonyl,  $\text{Rh}(\text{CO})_2$ , a linear species,  $\text{RhCO}$ , and a



multiply bonded species, Rh CO. The lower CO stretching vibration is associated with the multiply bonded species. The higher CO stretching vibration, which is resolved into components by infrared spectroscopy, contains the vibrations from the gem dicarbonyl and linear species. Though we cannot resolve these species in the CO stretching region, we can resolve them in a low frequency region. The peak at  $413\text{ cm}^{-1}$  is due to a bending vibration of the gem dicarbonyl, the peak at  $465\text{ cm}^{-1}$  is due to a bending vibration of the linear species (50). The frequencies found in this work with CO can all be slightly shifted by changes in adsorption temperature, particle size and the degree of surface saturation.

A number of experiments have been done to establish this identification. Figure 23 shows spectra for very low CO coverages on a surface with the rhodium coverage comparable to that of Fig. 21. Note that at the lowest CO coverages, the peak near  $465\text{ cm}^{-1}$  appears and only at higher coverages does the saturation profile with a stronger peak at  $413\text{ cm}^{-1}$  appear. A simple interpretation is that at the lowest coverages, linear CO formed on sites that could accommodate 2 CO molecules and, in fact, do at saturation.

Another experiment is to go to very low rhodium coverages. Under these conditions, infrared workers have found that predominantly the gem dicarbonyl species is formed. In Figure 24 the lower trace, labeled by 0%, shows only the  $413\text{ cm}^{-1}$  peak assigned as the gem dicarbonyl in agreement with the infrared results. This figure also shows that with the addition

of sulfur, the gem dicarbonyl sites can be selectively poisoned to sites that will only adsorb linear CO as shown by the growth of the peak near  $465\text{ cm}^{-1}$  at the expense of the peak near  $413\text{ cm}^{-1}$  (51).

This is an observation that has only been made with tunneling spectroscopy but should be accessible to infrared spectroscopy. Specifically, the prediction is that sulfur poisoning will preferentially inhibit gem dicarbonyl formation and will convert gem dicarbonyl sites to linear sites.

One of the main reasons for studying carbon monoxide adsorbed on transition metals is to understand the catalytic hydrogenation of carbon monoxide to form hydrocarbons, including synthetic fuels. Figure 25 shows tunneling spectra for CO on alumina supported rhodium that is heated in the presence of hydrogen. The bottom spectrum was run in the usual manner. Then the junction was removed from the storage dewar and warmed to room temperature by blowing compressed air on it. It was placed in a small, higher pressure cell made from a pipe fitting tee. It was pressurized to approximately 2000 Psi of hydrogen and then heated by means of a heating tape wrapped around the tee. Note that after heating to 380K, the gem dicarbonyl has decreased and there is a trace of a vibrational mode between 0.3 and 0.4 electron volts: the CH stretching region. As the cycle was repeated with heating to successively higher temperatures, the peaks due to adsorbed carbon monoxide continued to decrease in intensity while the peaks due to hydrocarbons increased in intensity (52).

Figure 26 shows a differential spectra of the resultant hydrocarbon with its peaks numbered. Though it may appear from this spectra that the

peaks are easily confused with noise, in fact they are reproducible as can be seen in the blown-up version shown in Fig. 27. In this spectrum we show the effects of starting with different carbon monoxide isotopes.

Note that the spectra are the same for  $^{12}\text{C}^{16}\text{O}$  and  $^{12}\text{C}^{18}\text{O}$ . This suggests that the hydrocarbon that is forming does not include the oxygen from the carbon monoxide in its structure. In contrast, the upper spectrum which started with  $^{13}\text{C}^{16}\text{O}$  shows definite shifts, showing that the carbon in the hydrocarbon originated from the carbon monoxide; the hydrocarbon was not an impurity.

The identification of this hydrocarbon was challenging. There were no vibrational spectra for model hydrocarbons on rhodium. The best set of model compounds we could find were halogenated hydrocarbons, hydrocarbons bound to chlorine, and bromine atoms. At first, this may seem a poor choice for model compounds but, in fact, it turns out to be adequate. The stretching force constant in a carbon-rhodium bond and a carbon-halogen bond turn out to be nearly the same. Of course, the mass must be corrected for, but this can be done by extrapolating between results for iodine and bromine since rhodium is intermediate in mass between that of iodine and bromine.

Figure 28 shows three possibilities for what the unknown could be. The position of the unknown peaks are lettered and numbered to correspond to Fig. 26. The position of the halogenated compound's peaks are shown by circles with dots in them. The position of the unknown between the iodine and the bromine is scaled according to the square root of the mass of the rhodium. Note that the agreement between the unknown peaks and the peaks

for a methyl group is poor. The unknown has peaks where the methyl group does not have peaks. The addition of a  $\text{CH}_2$  group increases the number of

modes to rough agreement but the position is still poor; in particular, the unknown has peaks where the  $\text{CH}_2\text{CH}_3$  does not have peaks and  $\text{CH}_2\text{CH}_3$  has

peaks where the unknown does not have peaks. However, the ethylidene species,  $\text{CHCH}_3$ , agrees both in number and position remarkably well with

the unknown. This agreement, coupled with the isotope shift measurements, and other attempted fits to the data, led us to conclude that the CO was hydrogenated to form a stable ethylidene species (53). This is the first observation, to our knowledge, of the formation of this species from the hydrogenation of CO on any supported metal catalyst.

It is of interest that this two carbon species could be formed without the addition of more CO in the gas phase. Thus, it was probably not produced by CO insertion. A possible mechanism would be from the polymerization of  $\text{CH}_2$  groups from dissociated CO that had been hydrogenated.

We then proceeded to other transition metals to see what differences we would find from the rhodium results. Figures 29 and 30 show carbon monoxide adsorbed on iron particles supported on alumina. From the isotope shifts shown in Fig. 30, we were able to conclude that the bottom two vibrational modes are due to bending vibrations, the upper to a stretching vibration (54). This is in marked contrast to the situation for iron pentacarbonyl in which most of the bending vibrations are at higher energies than the stretching vibrations. This apparent contradiction can be resolved in the work on substituted iron carbonyls, it showed that as the number of CO molecules per iron atom decreases, the stretching modes

increase in frequency while the bending modes decrease in frequency. In fact, extrapolation of the trends puts the modes in the range we observe for one CO per iron atom. This illustrates the dangers in using carbonyl data carelessly to assign low frequency vibrational modes of species on supported metal catalysts.

An interesting feature of this data is the relatively large intensity of the bending modes to the stretching modes. This feature is even more prominent for the rhodium results discussed above. Why? Possibilities include: 1) That the coupling of tunneling electrons to the bending modes is intrinsically stronger than the coupling to stretching modes. This seems improbable based on both experiments with other compounds and theory. 2) That an orientational effect is enhancing the bending modes. Such an orientational effect could be peculiar to the geometry of the metal electrode on top of metal particles; for example, most of the inelastic electron tunneling could take place near the edges of the particles. The results could be easily understood, however, if the CO were inclined relative to the metal particle's surface. This inclination could be due to an interaction of the  $\pi$  electrons or the oxygen atom with the metal surface and may be important for understanding CO dissociation.

When we heated the CO on iron in an attempt to hydrogenate the CO, hydrocarbons were formed, but in much smaller yields than on rhodium. See Fig. 31. In part, this is due to our inability to make junctions with large amounts of iron. Junctions had large background structures, possibly due to magnetic anomalies at large iron coverages. At any rate, we have not to date been able to produce sufficient quantities of hydrocarbons for CO on alumina supported iron to warrant identification.

The situation is similar on cobalt. Figure 32 shows the spectrum for CO on cobalt with different isotopes that allow the sorting and assignment of the CO vibrational modes, but as shown in Fig. 33, when the CO is heated in hydrogen, or in this case a hydrogen-CO gas mixture (synthesis gas), very small yields of hydrocarbons have been obtained.

Figures 34 and 35 show results for CO on nickel on alumina (55). CO on nickel on alumina gives a large number of species that have been extensively studied in the CO stretching region by infrared spectroscopy. Figure 34 shows four different species with the types of shifts with coverage that have been much discussed in the infrared literature. Figure 35 shows the low frequency modes. When these samples are heated in synthesis gas, only minute traces of hydrocarbons are found as shown in Fig. 36. This may be consistent with nickel's tendency to produce primarily methane. We might expect that the larger hydrocarbons such as the ethylidene found on rhodium simply are not produced on nickel.

#### IV. COMPARISON OF TUNNELING SPECTROSCOPY TO INFRARED AND ELECTRON ENERGY LOSS SPECTROSCOPY

Figure 37 compares results on the same model system, CO on rhodium on aluminum oxide, from three different experimental techniques. The upper trace shows the infrared results, which are well resolved in the CO stretching region, but nonexistent in the low frequency region. The analysis of this type of data has yielded a great deal of important information about catalysts. The real question is whether inelastic tunneling spectroscopy can supplement the results found by infrared spectroscopy. We have discussed already the tunneling spectrum shown in the middle trace. The bottom trace is an electron energy loss spectra

found in the recent work of Dubois et al (47). This sample was prepared by evaporating rhodium onto oxidized aluminum from the same type of filaments, with the same experimental geometry as used in tunneling experiments.

Electron energy loss spectroscopy is destined to become an important tool in analyzing adsorbed species on model catalysts. Will tunneling spectroscopy be important? It may, based on its ability to give high enough resolution spectra in the low energy region to allow isotope shift measurements of peak positions for assignment. We have found these isotopic shifts invaluable for obtaining unambiguous assignments of vibrational modes. What seems to be needed at this point is the use of tunneling spectroscopy in conjunction with the more conventional catalysis techniques to give an overall picture of a catalytic reaction.

#### V. SUMMARY

Inelastic tunneling spectroscopy has a spectral range that includes all molecular vibrations. Its sensitivity is sufficient to observe a fraction of a monolayer; its resolution, while not theoretically limited, is practically limited to the range of 1 to 4 millielectron volts (8-30

<sup>-1</sup> cm ). Both Raman and infrared active modes are observed. There is a slight orientational preference for modes oscillating perpendicular to the direction of the tunneling electrons.

Problems with tunneling spectroscopy include uncertainties introduced by the top metal electrode, cryogenic temperatures and perhaps most important that actual catalysts cannot be studied. Model systems must be fabricated.

Model systems that have been actively studied include oxidized alumina as a model for  $\gamma$ -alumina, oxidized magnesium as a model for magnesia, evaporated transition metals on oxidized aluminum and magnesium as models for supported metal catalysts, and deposited cluster compounds as a model for supported cluster catalysts.

Some representative results that have been obtained in our laboratory are: 1) CO adsorbed on rhodium can be hydrogenated to form a two carbon species without the addition of gas phase CO. Thus, a two carbon species can be formed without CO insertion. 2) Linearly bonded  $\text{RhCO}$  is relatively inactive during hydrogenation. It persists after the gem dicarbonyl  $\text{Rh}(\text{CO})_2$  and multiply bonded  $\text{Rh}_x\text{CO}$  have disappeared with the formation of hydrocarbons. 3) Sulfur poisoning converts the more active gem dicarbonyl sites into the relatively inactive linear sites. 4) An unusually high intensity for bending modes in several systems, especially CO on Rh, suggests the possibility of bent over CO.

#### VI. ACKNOWLEDGMENTS

We thank A. Bayman, R. V. Coleman, S. de Cheveigne, J. Hall, W. C. Kaska, D. McBride, G. Walmsley, and H. Weinberg for figures and helpful discussions. This work was in part supported by the Office of Naval Research and National Science Foundation Grant DMR76-83423.



## VII. APPENDIX

A. Experimental Techniques

Since the techniques for fabricating tunnel junctions are unfamiliar to the majority of catalysis researchers, we give here a summary of the techniques and procedures involved in junction formation and testing. More information can be obtained in other review articles and papers (4-10).

Tunneling junctions are fabricated in high vacuum evaporators. The aluminum metal is evaporated from three-stranded tungsten filaments; aluminum wire of order 1/10 mm can simply be wrapped around a  $3 \times 0.04$ " stranded tungsten filament and heated to evaporate. The lead can be evaporated from a variety of boats, including tantalum, tungsten, and molybdenum. We prefer molybdenum with tantalum a close second.

Most transition metals can be evaporated from stranded tungsten filaments provided that only a small charge of the transition metal (not exceeding about 5% by weight) is simply wrapped around  $3 \times 0.025$ " stranded tungsten wire. In this way, we have successfully evaporated iron, nickel, cobalt, rhodium, platinum and palladium.

The thickness of the metal electrodes can be monitored by a commercial oscillating quartz crystal film thickness monitor, though for the very thin layers of transition metal, we prefer to drive the crystal and simply count the frequency directly with a commercial frequency counter. Optimal source to substrate distances are probably in the range of 5 to 10 inches. The further the substrate is from the source, the cooler it will remain during evaporation and the more uniform the

deposition will be, but the amount of material used for a given thickness increases roughly as the square of the distance to the substrate. Since the amount of material that can be wrapped around tungsten filaments is limited, it is good to keep the source as close to the substrate as consistent with required uniformity. We tend to use about 6 inches.

The patterns of the electrodes are defined by machined or electroformed masks. The mask material can be either aluminum or stainless steel; brass should be avoided because of possible zinc sublimation.

The substrates for the evaporation vary from group to group from fused alumina to ordinary glass microscope slides. We use the ordinary glass microscope slides.

For catalysis measurements, freedom from unwanted hydrocarbon contamination is a constant problem. Precautions must begin with careful cleaning of the substrates and of anything placed in the vacuum chamber. We have found that detergent washing, followed by thorough water rinsing, followed by deionized water rinsing, followed by drying with heat guns is a sufficient cleaning procedure.

The vacuum chamber itself can be cleaned by the washing described above and maintained clean either by the use of foreline traps on mechanical pumps and glow discharge cleaning with argon or by using only oil-free pumping systems. Typical glow discharge parameters would be 100 milliamps at 400 volts for 5 minutes, with a glow maintained between an aluminum electrode and the chamber walls.

The sequence of steps for fabricating a tunnel junction is: 1) An

aluminum electrode approximately 700 Angstroms thick is deposited on the glass substrate. 2) This aluminum electrode is then oxidized either by glow discharge (22) or thermal oxidation in air. For the supported metal samples discussed in this paper, we use an oxidation in air at 200° for 10 minutes. For junctions to be doped with larger hydrocarbons, such extensive oxidation is unnecessary. A brief exposure to air at room temperature or a brief glow discharge oxidation are sufficient. 3) The junction is then doped, either by dropping on a liquid solution and spinning the excess (56), by dipping the junction into the solution and shaking off the excess (57), by vapor exposure in the vacuum chamber (58), or by evaporating onto it complexes or particles of transition metals in controlled pressures of gases such as CO. The temperature of the substrate is often varied to aid the doping process. 4) The junctions are completed with an evaporated lead electrode with a thickness in the range 700-3000 Angstroms. 5) Junctions are tested with a low power ohmmeter and, if necessary, the substrate is trimmed to size for insertion into the measuring apparatus.

The most critical steps in junction fabrication are the formation of the barrier and its doping. The formation of oxide barriers has been studied in some detail by Bowser and Weinberg (22) and by Magno and Adler (59). Some work has been done on non-oxide barriers (60), but rapid conductance changes with voltage make it difficult to see inelastic tunneling peaks. Evans, Bowser, and Weinberg have recently applied X-ray photoelectron spectroscopy to characterize the alumina barriers used in tunneling spectroscopy (61).

The doping of the barriers by vapor exposure or liquid exposure

must basically be discussed on a case by case basis in the research papers themselves. One new technique that has not yet been applied to catalysis studies, but has great potential, is infusion doping (62,63). Here dopants are infused into completed junctions. Surprisingly, dopants as large as naphthanol have been infused. We can expect to see more studies involving the reaction of an adsorbed species with an infused species in the future. This has already been done for hydrogen (53) and hydrogen sulfide (51), but the potential exists for a wide range of infused species.

### B. Cryogenics

Most of the measurements reported in this review were taken at 4.2K. This temperature can be achieved by simply inserting the sample down the neck of a vendor supplied storage dewar on a probe similar to that shown in Fig. 6. Lower temperatures, for higher resolution, can be obtained by pumping on liquid helium in conventional research dewars. The lowest temperature used to date was below 0.1 K, obtained in a helium dilution refrigerator (5).

### C. Electronics

The basic concept for measuring the tunneling spectra is simple. See Fig. 38. The current vs. voltage curve is run with a voltage range of order -5 to +5 millivolts to look for the superconducting energy gap of the lead metal electrode and insure that the current flow is due to tunneling. After this, the junction is fed with the sum of a dc current and ac modulation current. These currents are best supplied by voltage sources in series with large resistors. Actual current sources should be avoided because of their intrinsically higher noise. A voltage source in series with a large resistor has its output noise divided between the

relatively small junction resistance and the high series resistance. A true current source puts all of its output noise across the junction. The voltage across the junction is measured usually with a differential volt meter and the x-axis of a chart recorder. Then a component of the voltage is measured at the first harmonic frequency (1120 Hz in our measurements) to set the modulation voltage at the desired level, which is generally between 0.7 and 2 millivolts. Then the lock-in amplifier is used to measure the second harmonic voltage. For this measurement, the first harmonic voltage must be attenuated in some way. Modern lock-in amplifiers can be purchased with sufficient input filtering to reject the first harmonic voltage with no external circuitry. Circuitry has been described to help lock-in amplifiers with this rejection task (64). It should be remembered, however, that no active devices should be used since the noise level in the measurement of the second harmonic voltage is critical. That noise is what limits the speed with which tunneling spectra can be recorded. In this same light, it is important not to apply the dc voltage across the junction directly to the input of a digital volt meter or chart recorder. These inputs typically put too much noise back across the junction, which appears at the input to the lock-in amplifier. Thus, it is important to put the dc voltage through a quiet buffer amplifier (e.g., PAR 113 or homebuilt voltage follower).

## VIII. REFERENCES

- [1] R.C.Jaklevic and J.Lambe, Physical Review Letters 17, 1139-1140 (1966)
- [2] J.Lambe and R.C.Jaklevic, Physical Review 165, 821-832 (1968)
- [3] S.Colley and P.K.Hansma, Review Scientific Instruments 48, 1192-1195 (1977)
- [4] P.K.Hansma, Physics Reports 30C, 145-206 (1977)
- [5] W.H.Weinberg, Annual Review Physical Chemistry 29, 115-139 (1978)
- [6] P.K.Hansma and J.Kirtley, Accounts Chemical Research 11, 440-445 (1978)
- [7] T.Wolfram, ed., in: Inelastic Electron Tunneling Spectroscopy (Springer-Verlag, New York, 1978)
- [8] R.G.Keil, T.P.Graham and K.P.Roenker, Applied Spectroscopy 30, 1-18, (1976)
- [9] P.N.Shott and B.O.Field, Surface Science and Interface Analysis 1, 63-70 (1979)
- [10] N.M.Brown and D.G.Walmsley, Chemistry in Britain 12, 92-94 (1976)
- [11] R.M.Kroeker and P.K.Hansma, Surface Science 67, 362-366 (1977)
- [12] D.G.Walmsley, R.B.Floyd and S.F.J.Read, Journal Physics C: Solid State Physics, 11, L107-L110 (1978)
- [13] J.Kirtley and P.K.Hansma, Physical Review B 13, 2910-2917 (1976)
- [14] M.G.Simonsen and R.V.Coleman, Journal Chemical Physics 61, 3789-3799 (1974)
- [15] D.A.Causs, H.L.Strass and P.K.Hansma, Science 192, 1128-1130 (1976)
- [16] J.T.Hall and P.K.Hansma, Surface Science 71, 1-14 (1978)
- [17] J.Kirtley and P.K.Hansma, Surface Science 66, 125-130 (1977)
- [18] I.W.N.McMorris, N.M.D.Brown and D.G.Walmsley, Journal Chemical

Physics 66, 3952-3961 (1977)

- [19] A.Bayman, W.C.Kaska and P.K.Hansma, manuscript in preparation
- [20] K.W.Hipps and U.Mazur, Journal Physical Chemistry, in press
- [21] P.K.Hansma, D.A.Hickson and J.A.Schwarz, Journal Catalysis 48, 237-242 (1977)
- [22] W.M.Bowser and W.H.Weinberg, Surface Science, 64, 377-392 (1977)
- [23] J.T.Hall and P.K.Hansma, Surface Science, 76, 61-76 (1978)
- [24] N.M.D.Brown, R.B.Floyd and D.G.Walmsley, Journal Chemical Society Faraday Transactions II, 75, 17-31 (1979)
- [25] N.M.D.Brown, W.J.Nelson and D.G.Walmsley, Ibid., 75, 32-39 (1979)
- [26] N.M.D.Brown, D.G.Walmsley and R.B.Floyd, Journal Catalysis, 52, 347-352 (1978)
- [27] O.I.Shklyarevskii, A.A.Lysykh and I.K.Yanson, Soviet Journal Low Temperature Physics, 2, 328-333 (1976)
- [28] A.F.Diaz, U.Hetzler and E.Kay, Journal American Chemical Society, 99, 6780-6781 (1977)
- [29] R.C.Jaklevic, Applications Surface Science 4, 174-182 (1980)
- [30] D.E.McBride and J.T.Hall, Journal Catalysis 58, 320-327 (1979)
- [31] H.E.Evans and W.H.Weinberg, Journal Chemical Physics 71, 4789-4798 (1979)
- [32] N.M.D.Brown, W.E.Timms, R.J.Turner and D.G.Walmsley, Journal Catalysis, 64, 101-109 (1980)
- [33] M.F.Muldoon, R.A.Dragoset and R.V.Coleman, Physics Reports B, 20, 416-429 (1979)
- [34] M.K.Konkin, R.Magno and J.G.Adler, Solid State Communications, 26, 949-952 (1978)
- [35] D.G.Walmsley, R.B.Floyd and W.E.Timms, Solid State Communications,

- 22, 497-499 (1977)
- [36] R.Magno and J.G.Adler, Surface Science, 78, L250-L256 (1978)
- [37] R.B.Floyd and D.G.Walmsley, Solid State Physics, 11, 4601-4614 (1978)
- [38] D.G.Walmsley, W.J.Nelson, N.M.D.Brown and R.B.Floyd, Applications Surface Science 5, 107-120 (1980)
- [39] C.S.Korman, J.C.Lau, A.M.Johnson and R.V.Coleman, Physical Review B 19, 994-1014 (1979)
- [40] H.E.Evans and W.H.Weinberg, Journal American Chemical Society 102, 872-873 (1980)
- [41] H.E.Evans and W.H.Weinberg, Ibid., 102, 2548-2553 (1980)
- [42] H.E.Evans and W.H.Weinberg, Ibid., 102, 2554-2558 (1980)
- [43] H.E.Evans and W.H.Weinberg, Journal Vacuum Science Technology, 17, 47-48 (1980)
- [44] K.W.Hipps, U.Mazur and M.S.Pearce, Chemical Physics Letters, 68, 433-437 (1979)
- [45] W.M.Bowser and W.H.Weinberg, Journal American Chemical Society, in press
- [46] H.E.Evans, W.M.Bowser and W.H.Weinberg, Surface Science 85, L497-L502 (1979)
- [47] L.H.Dubois, P.K.Hansma and G.A.Somorjai, Applications of Surface Science, in press
- [48] J.Klein, A.Leger, S. de Cheveigne, C.Guinet, M.Belin and D.Defourneau, Surface Science 82, L288-L292 (1979)
- [49] S. de Cheveigne, Thesis at the University of Paris VII, (1980)
- [50] R.M.Kroeker, W.C.Kaska and P.K.Hansma, Journal Catalysis 57, 72-79 (1979)



- [51] R.M.Kroeker, W.C.Kaska and P.K.Hansma, Journal Catalysis 63, 487-490 (1980)
- [52] P.K.Hansma in: Inelastic Electron Tunneling Spectroscopy, T.Wolfram ed., (Springer-Verlag, New York 1978) p. 186
- [53] R.M.Kroeker, W.C.Kaska and P.K.Hansma, Journal Catalysis 61, 87-95 (1980)
- [54] R.M.Kroeker, W.C.Kaska and P.K.Hansma, Journal Chemical Physics 72, 4845-4852 (1980)
- [55] R.M.Kroeker, W.C.Kaska and P.K.Hansma, Journal Chemical Physics, in press
- [56] P.K.Hansma and R.V.Coleman, Science 184, 1369-1371 (1974)
- [57] Y.Skarlatos, R.C.Barkar and G.L.Haller, Surface Science 43, 353-368 (1974)
- [58] M.G.Simonsen and R.V.Coleman, Physical Review B 8, 5875-5887 (1973)
- [59] R.Magno and J.G.Adler, Physical Review B, 13, 2262-2269 (1976)
- [60] R.Magno and J.G.Adler, Physical Review B, 15, 1744-1750 (1977)
- [61] H.E.Evans, W.M.Bowser, W.H.Weinberg, Applications of Surface Science, 5, 258-274 (1980)
- [62] R.C.Jaklevic and M.R.Gaerttner, Applications Surface Science, 1, 479-502 (1978)
- [63] R.C.Jaklevic and M.R.Gaerttner, Applied Physics Letters, 30, 646-648 (1977)
- [64] D.E.Thomas and J.M.Rowell, Review Scientific Instruments 36, 1301-1306 (1965)

## FIGURE CAPTIONS

Figure 1. The harmonic oscillator of the idealized picture is one of the vibrational modes of a dopant molecule in the actual junction. Each vibrational mode of the dopant molecule is revealed as a peak in  $d^2V/dI^2$  at a voltage  $V=hv/e$ . The tunneling spectrum can be directly compared to infrared and Raman spectra: 0.1 V corresponds to  $806.5 \text{ cm}^{-1}$ . From reference 6.

Figure 2. The low energy modes of three acids chemisorbed on the alumina are compared. Notice that the frequency range extends to 0 meV. These spectra are the difference spectra between doped and undoped junctions taken at 4.2 K with an applied magnetic field.

Figure 3. Methanesulfonate tunneling spectrum. The weak selection preference for vibrations that are perpendicular to the oxide surface can be seen by comparing the symmetric ( $\nu_s$ ) and antisymmetric ( $\nu_a$ ) modes of the same vibrational group on this molecule with known orientation. From reference 6.

Figure 4. Observed peak shifts for various vibrational modes are generally found to be less than one percent of their reported non-tunneling values. Exceptions are small molecules with large dipole derivatives such as OH and CO.

Figure 5. The top electrode has been found to have a large effect on the low energy modes of CO chemisorbed on iron. From these preliminary results found by Atiye Bayman it is seen that the frequencies found for small molecules with large dipole derivatives such as CO depend on the nature of the top electrode.

Figure 6. Photograph of probe used to immerse the junctions in liquid helium for measurement at 4.2 K. Handling of cryogenic material is avoided by simply inserting the probe into a storage dewar. The use of brass screw clamps to contact the electrodes simplifies attachment and avoids heating due to soldering.

Figure 7. The geometry of the tunnel junctions gives rise to a severe restriction on the thickness of the samples to be studied, represented by the question marks in the figure. Commercial catalysts can not be used directly but instead must have their essential features simulated in model catalyst systems.

Figure 8. Electron micrograph of small Al particles formed by the evaporation of Al metal in argon at a pressure of 10 Torr. The particles were oxidized in air and studied with standard catalyst evaluation techniques to characterize the oxide that grows on Al metal. See reference 21.

Figure 9. IET spectra for chemisorbed propiolic acid (curve A) is seen to change after a period of time of two weeks, or heating to 175°C for a few minutes, to that of curve B. This is compared to the spectrum of chemisorbed acrylic acid (curve C). The stick spectrum shows the IR and Raman frequencies for sodium acrylate. From reference 29.

Figure 10. Spectra of two muconic acid doped junctions. After doping, the oxidized aluminum strips were heated in 0.3 Torr of  $D_2O$  vapor, the strip in trace A to  $50^\circ C$  and the strip in trace B to  $325^\circ C$ . From reference 30.

Figure 11. Spectra of a) 1-hexyne, b) 3-hexyne and c) 1-heptyne adsorbed onto plasma oxidized aluminum at room temperature. The spectra were taken at 2 K. From reference 32.

Figure 12. IET spectra, at 2 K, of a Mg-magnesium oxide-Pb tunnel junction doped with formic acid (top) and of an Al-aluminum oxide-Pb tunnel junction doped with formic acid. The arrow denotes the mode that has shifted down on magnesium oxide to coincide with another line. From reference 38.

Figure 13. IET spectra of typical aromatic-ring compounds adsorbed on  $MgO$ . (1) p-chlorobenzoic acid doped from ethanol, (2) 2-naphthoic acid doped from ethanol. The symmetric and antisymmetric stretches of the  $COO^-$  attachment group are indicated. From reference 39.

Figure 14. IET spectra of ethylene acetylene, and propylene on  $Zr(BH_4)_4/Al_2O_3$ . The peaks in the range  $2000-2500\text{ cm}^{-1}$  are associated with BH stretching; those in the range  $2850-3000\text{ cm}^{-1}$  are associated with CH stretching. From reference 41.

Figure 15. IET spectra in the range  $2700\text{ to }3100\text{ cm}^{-1}$  of ethanol chemisorbed on  $Ag/Al_2O_3$  for statistical Ag coverages of (a) 0, (b) 2.5, (c) 5.0, (d) 10.0 Angstroms. From reference 46.

Figure 16. A schematic view of model supported metal catalysts that can be

studied with tunneling spectroscopy. The supported particles are formed from metal vapor in vacuum directly on the oxide surface. The amount of metal deposited is generally measured with a quartz-crystal microbalance and reported as an average coverage.

Figure 17. Rhodium particles are shown in an electron micrograph of a specially prepared sample. The aluminum, evaporatively deposited and oxidized as in the preparation of a tunneling junction, is supported by a carbon-coated nickel grid. The relatively large crystallites are in the aluminum metal film. The oxide on the aluminum is too thin to be seen. The rhodium particles appear as small hemispheres with a typical diameter of 25 Angstroms.

Figure 18. Auger electron spectra of alumina, alumina with rhodium particles (evaporated from tungsten) and single crystal rhodium. No contamination of the rhodium by tungsten is observed for the evaporated particles. From reference 47.

Figure 19. IET spectra of  $^{12}\text{C}^{16}\text{O}$  and  $^{12}\text{C}^{18}\text{O}$  chemisorbed on alumina supported Rh (of average thickness 12 Angstroms). Peaks (1) and (1') are resolved only with 5 Angstroms or less of Rh (see inset). The peak at 115 meV is due to the alumina. From reference 48.

Figure 20. IET spectra for rhodium particles supported on magnesium oxide. The low frequency modes of chemisorbed CO are again observed. The rhodium coverage is that equivalent to a 4 Angstrom uniform layer. The rhodium is not uniform, but forms small particles on the magnesium oxide surface. From reference 49.

Figure 21. Differential spectra of CO chemisorbed on alumina supported rhodium particles. Peaks labeled are those due to CO. The small peak at 116 meV is due to the alumina support, and the peak near 445 meV is due to the OH groups in the junction. Peak positions are not corrected for possible shifts due the top lead electrode. Peak positions are found to vary with both rhodium coverage and CO exposure. From reference 50.

Figure 22. Differential IET spectra for CO chemisorbed on alumina supported rhodium particles. Spectrum (a) shows three modes; a bending vibration near 52 meV, a stretching vibration near 70 meV and a CO stretching mode near 243 meV. This species has been identified as due to two CO molecules linearly adsorbed per rhodium atom. Spectra (b,c,d,e) show the range of spectra obtained as the Rh/CO ratio, substrate temperature and particle size are varied to produce a second linear species. Spectrum (f) has a low energy bending mode near 58 meV and a stretching mode near 73 meV assigned to a linear Rh-CO species.

Figure 23. The low energy region of the model rhodium/alumina catalyst spectrum is shown for three different exposures to CO. The rhodium is in approx. 30 Angstrom diameter particles. For CO exposures of one Langmuir or less, a peak near 58 meV, due to Rh-CO, dominates. For higher CO exposures, a peak at 51.6 meV due to two CO molecules per rhodium atom rapidly becomes the most intense. From reference 51.

Figure 24. The low energy region of the model rhodium/alumina catalyst spectrum is shown for equal exposures to four mixtures of D<sub>2</sub>S and CO. The rhodium is highly dispersed so that exposure to 100% CO forms the dicarbonyl species with a bending mode at 51.6 meV. With increasing

$D_2S$  exposure a second peak near 60 meV also forms due to the adsorption of only one CO molecule per rhodium atom. From reference 51.

Figure 25. IET spectra showing repeated heatings of CO chemisorbed on rhodium/alumina. Heatings were done in a high pressure cell filled with  $H_2$  and CO. The loss of CO mode intensities and the growth of hydrocarbon modes with increasing temperatures is observed.

Figure 26. Differential IET spectra of  $^{13}CO$  on rhodium/alumina that has been heated to 420 K in hydrogen. Modes clearly due to hydrocarbon formation are numbered 1 to 7. Three other modes difficult to measure are present near 41, 60 and 117 meV. It is not known if the OH groups are on the alumina or the rhodium particles, or both. From reference 53.

Figure 27. IET spectra resulting from the use of three isotopes of CO to form hydrocarbons as in figures 25 and 26. In the region from 125 to 190 meV are the C-H deformation modes. No mode is seen to shift with heavy oxygen, but several modes are seen to shift with heavy carbon. This suggests that the hydrocarbon is formed from the carbon but not the oxygen of the chemisorbed CO. From reference 53.

Figure 28. Comparisons are shown between mode positions of the hydrocarbon formed in the tunneling junction and mode positions of known compounds. The vertical axis is scaled by the inverse square root of the mass of bromine, rhodium and iodine. It is also displaced for each set of compounds. Modes 1 to 6 of the hydrocarbon are observed directly. The measurement of the positions of modes A and B is

difficult due to overlap with other modes present. From the agreement with the two ethylidene species (and other tests) the hydrocarbon is identified as a  $\mu$ -ethylidene species. From reference 53.

Figure 29. Differential IET spectra of CO chemisorbed on alumina supported iron. Peaks labled by  $\text{cm}^{-1}$  are modes studied with isotopes. Peak positions have not been corrected for shifts due to the top lead electrode. From reference 54.

Figure 30. Differential IET spectra of the low frequency region for three isotopes of CO. Lines are drawn through measured positions for  $^{12}\text{C}^{16}\text{O}$ . Bending modes have a larger shift for  $^{13}\text{C}^{16}\text{O}$ , while stretching modes have a larger shift for  $^{12}\text{C}^{18}\text{O}$ . From reference 54.

Figure 31. Differential IET spectra of CO chemisorbed on alumina supported iron that has been heated in  $\text{H}_2$  and CO. Very little hydrocarbon is formed in the junction; the measured intensities are too small to allow assignment at present. Sintering of the iron particles causes a rapid rise in the background structure seen at low frequencies.

Figure 32. Differential IET spectra of CO chemisorbed on alumina supported cobalt particles. The three spectra show the effect of increasing cobalt coverages. The middle trace is for  $^{12}\text{C}^{18}\text{O}$ . The use of isotopes is invaluable in the identification of the observed modes.

Figure 33. Differential IET spectra of CO on cobalt/alumina that has been heated in  $\text{H}_2$  and CO. Hydrocarbons form in the junction in small amounts. From the modes that are observable, it is clear that this is a different species than that formed in junctions that contain rhodium



particles.

Figure 34. Differential IET spectra of CO chemisorbed on alumina supported nickel particles. Spectra show the desorption of the chemisorbed CO with increasing temperature for a completed junction. The thermal stability is found to be greatly increased by the top electrode. Note the downshifts in the frequency of the CO stretch modes after warming (and the resultant desorption of some CO). Indicated resolution is 3.9 meV. From reference 55.

Figure 35. Differential IET spectra of CO on nickel/alumina in the low frequency region. Many overlapping modes are observed from 43 to 67 meV. The indicated resolution is 2.6 meV. From reference 55.

Figure 36. Differential IET spectra of CO on nickel/alumina shown before and after heating in  $H_2$  and CO. Very little surface hydrocarbon is seen to form. This result may reflect the preference of nickel catalysts for methanation. From reference 55.

Figure 37. Comparison of three experimental techniques that can study alumina supported rhodium particles. The upper trace shows infrared results that are well resolved in the high frequency region but are non-existent in the low frequency range. The middle trace is the IET spectra of figure 21. The lower trace is an EEL spectra that has the full spectral range with limited resolution. It is seen that all three methods have complimentary features, and that no one technique yields all the information available. From reference 47.

Figure 38. Standard electronics for tunneling spectroscopy includes an

x-y chart recorder for recording tunneling spectra,  $d^2V/dI^2$  versus  $V$ , and an oscilloscope for measuring  $I$  versus  $V$  as a check on junction quality. From reference 4.

## TABLE CAPTION

Table 1. The resolution of a tunneling spectrum is largely determined by the temperature and modulation voltage. Although there is no fundamental limit to resolution, the time to take a spectrum at the same signal to noise ratio increases rapidly with increasing resolution. The trace times are for three different time constants on the lock-in amplifier measuring the y-axis signal; the times shown allow roughly six time constants per resolution element in a 0 to 0.5 eV spectrum.

Superconductivity in the electrodes will slightly improve resolution over the values listed here, and will shift the peaks. The values listed are for an Al-I-Pb junction.

FIGURE 1

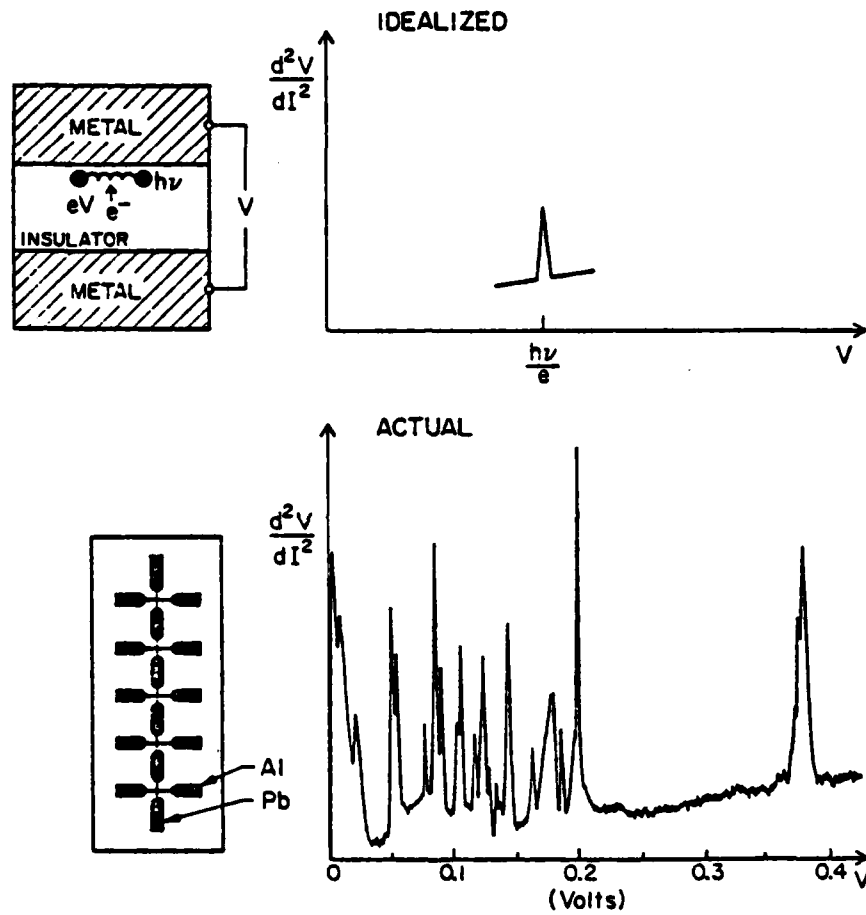


FIGURE 2

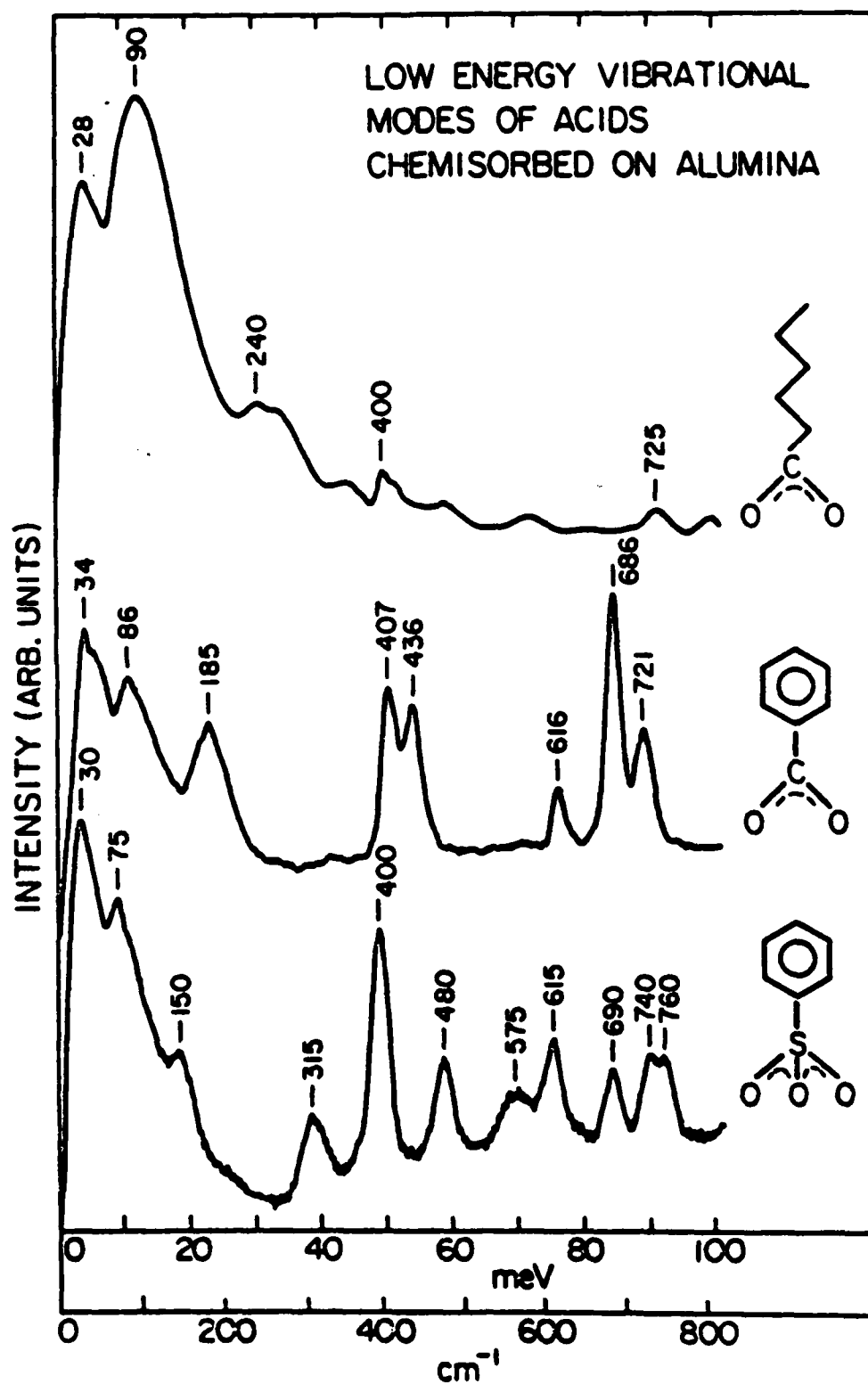


FIGURE 3

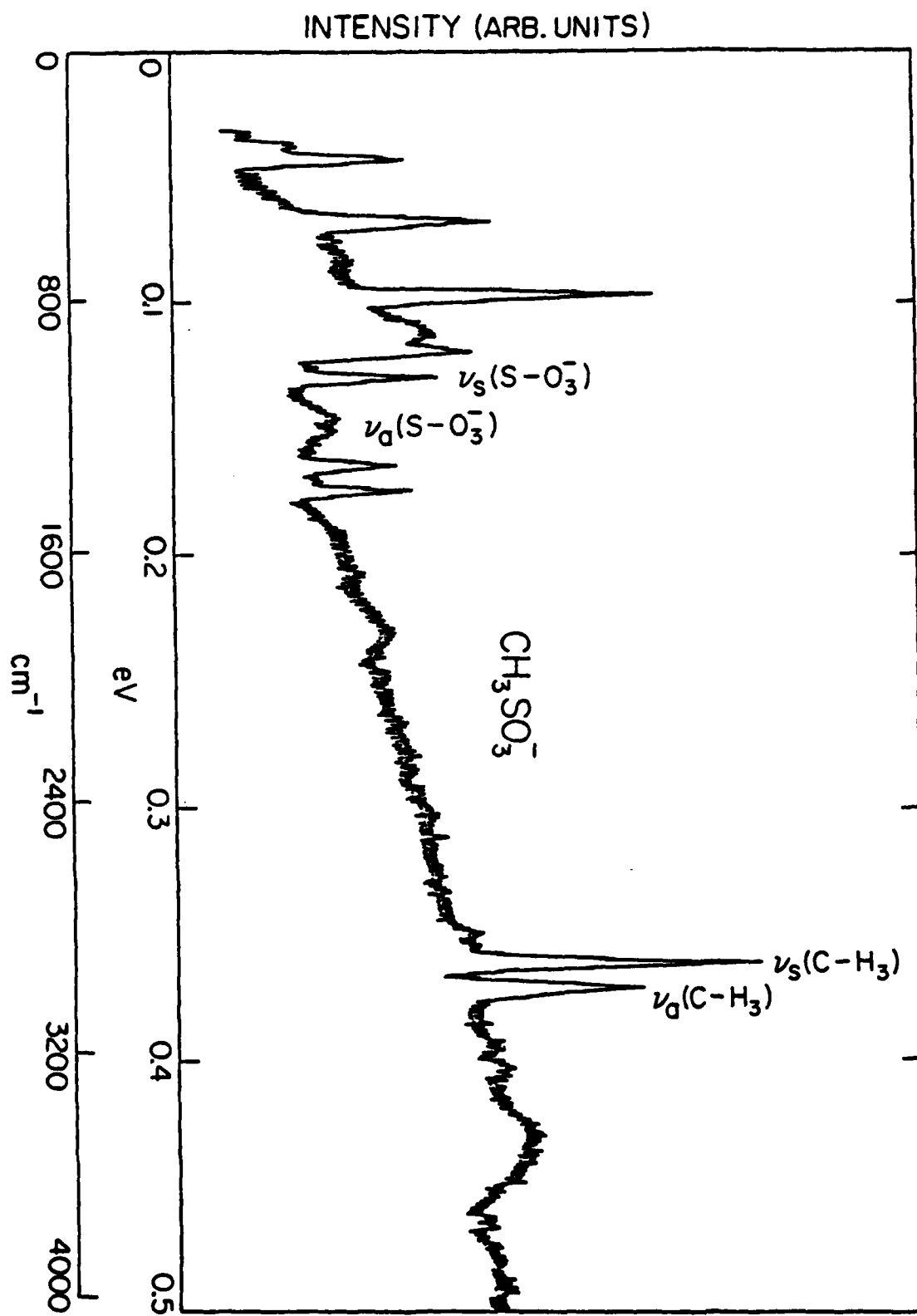


FIGURE 4

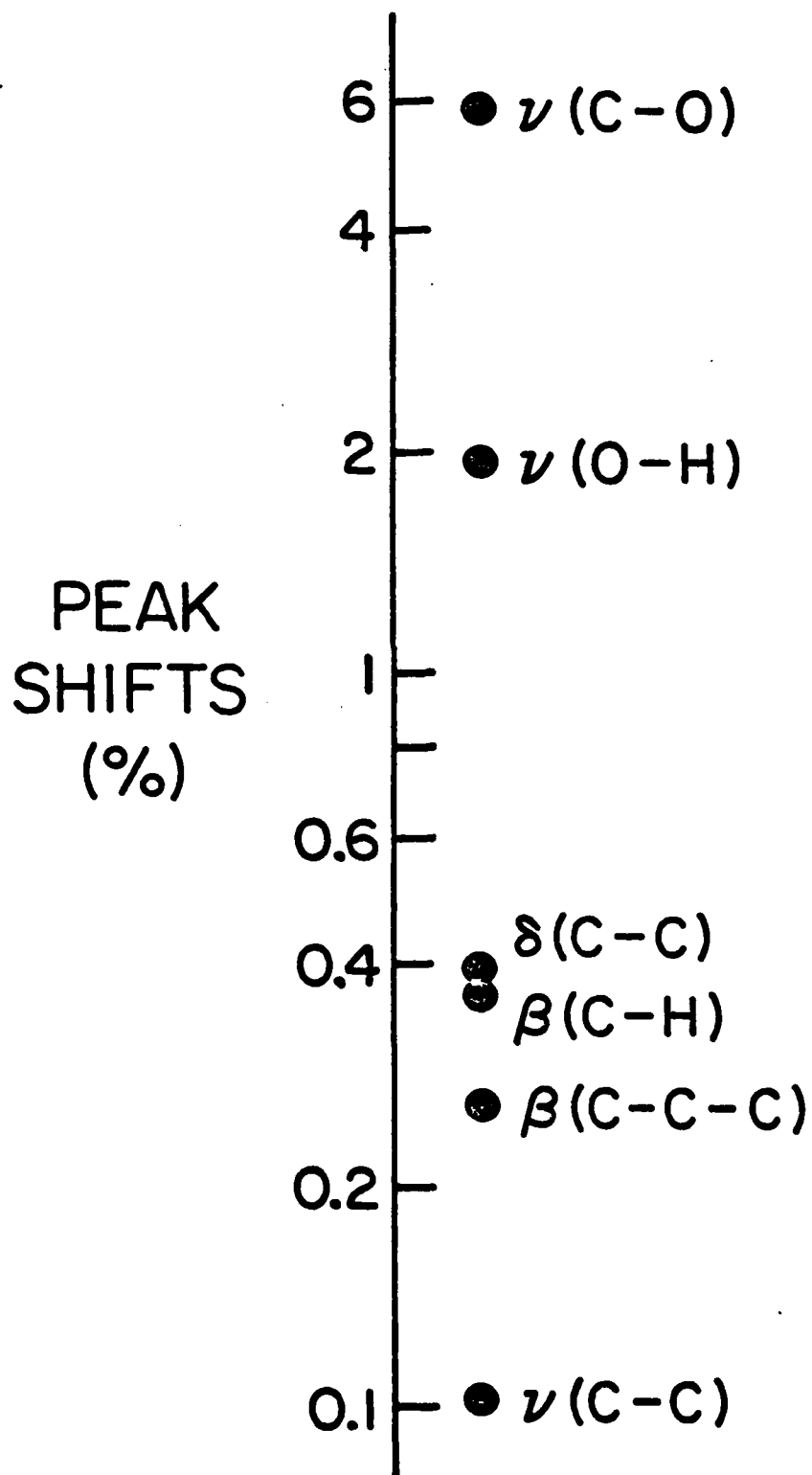


FIGURE 5

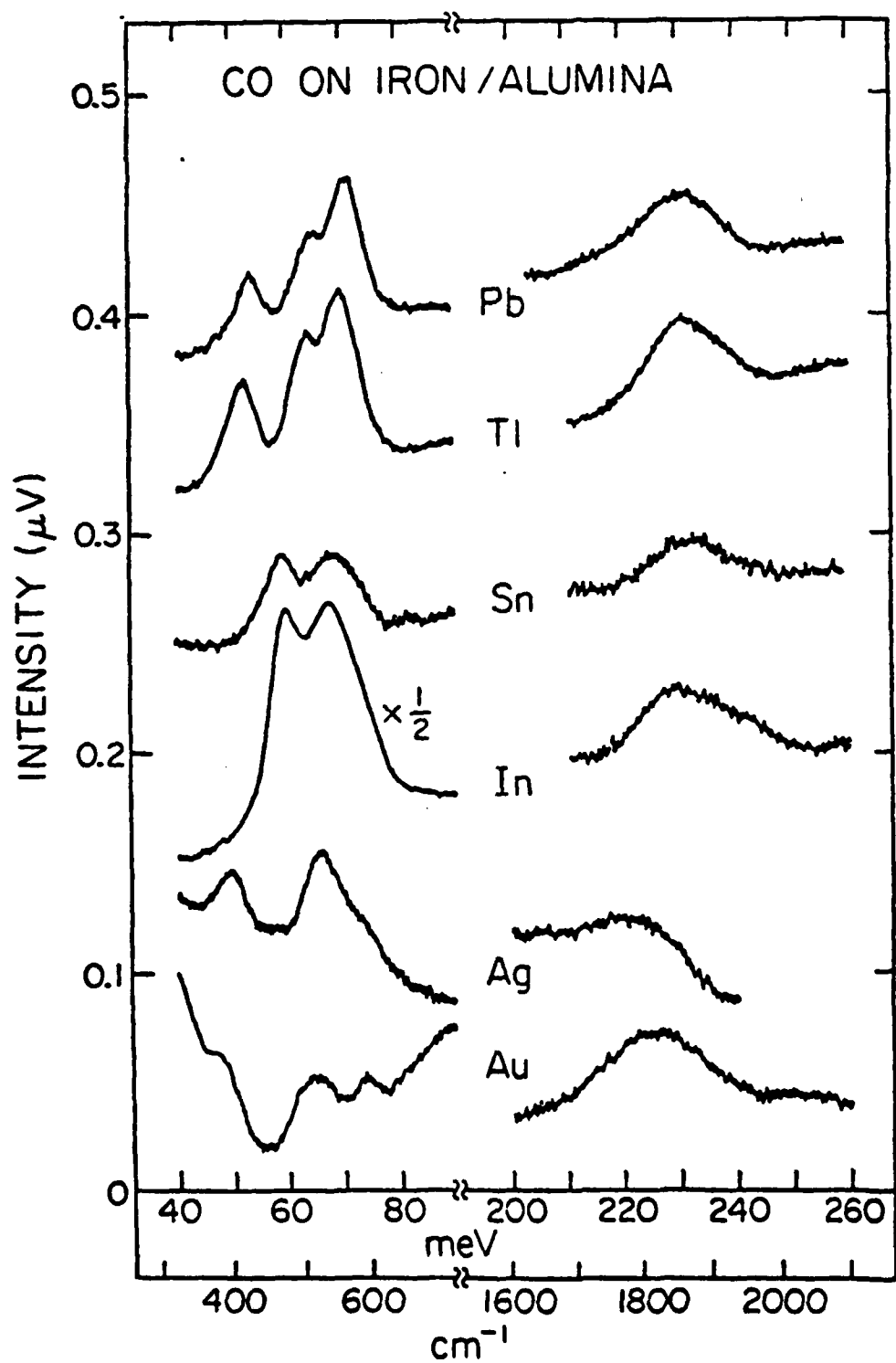




FIGURE 6

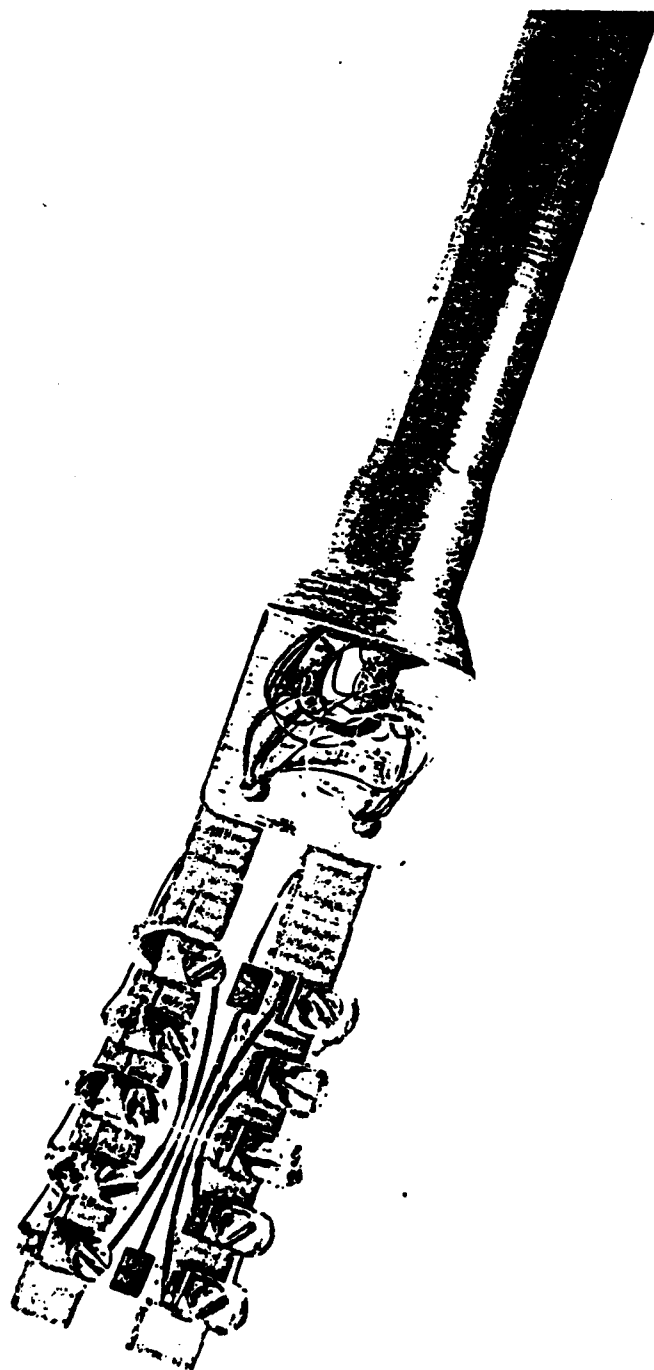


FIGURE 7

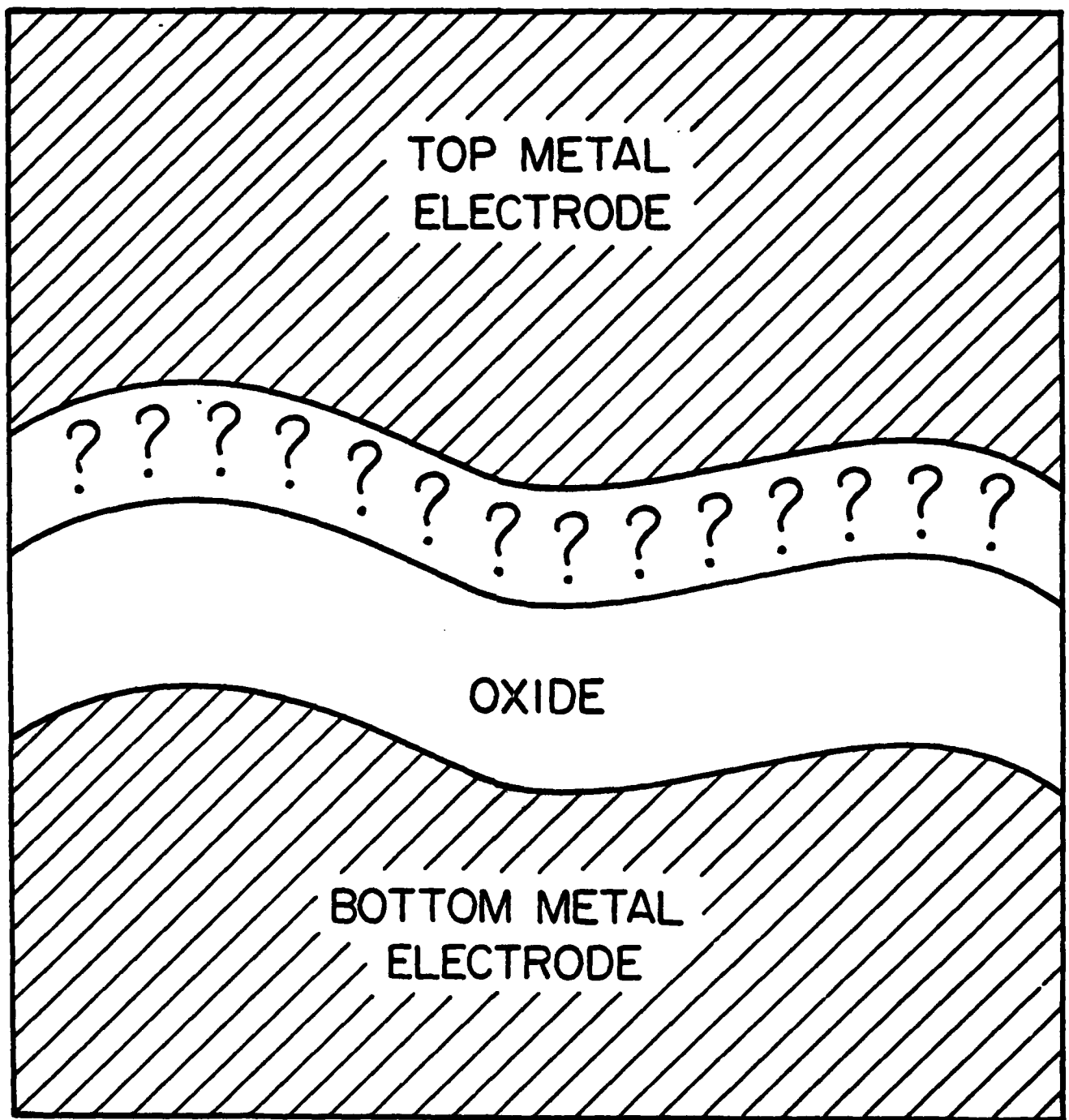


FIGURE 8



FIGURE 9

Al - Pb 4°K

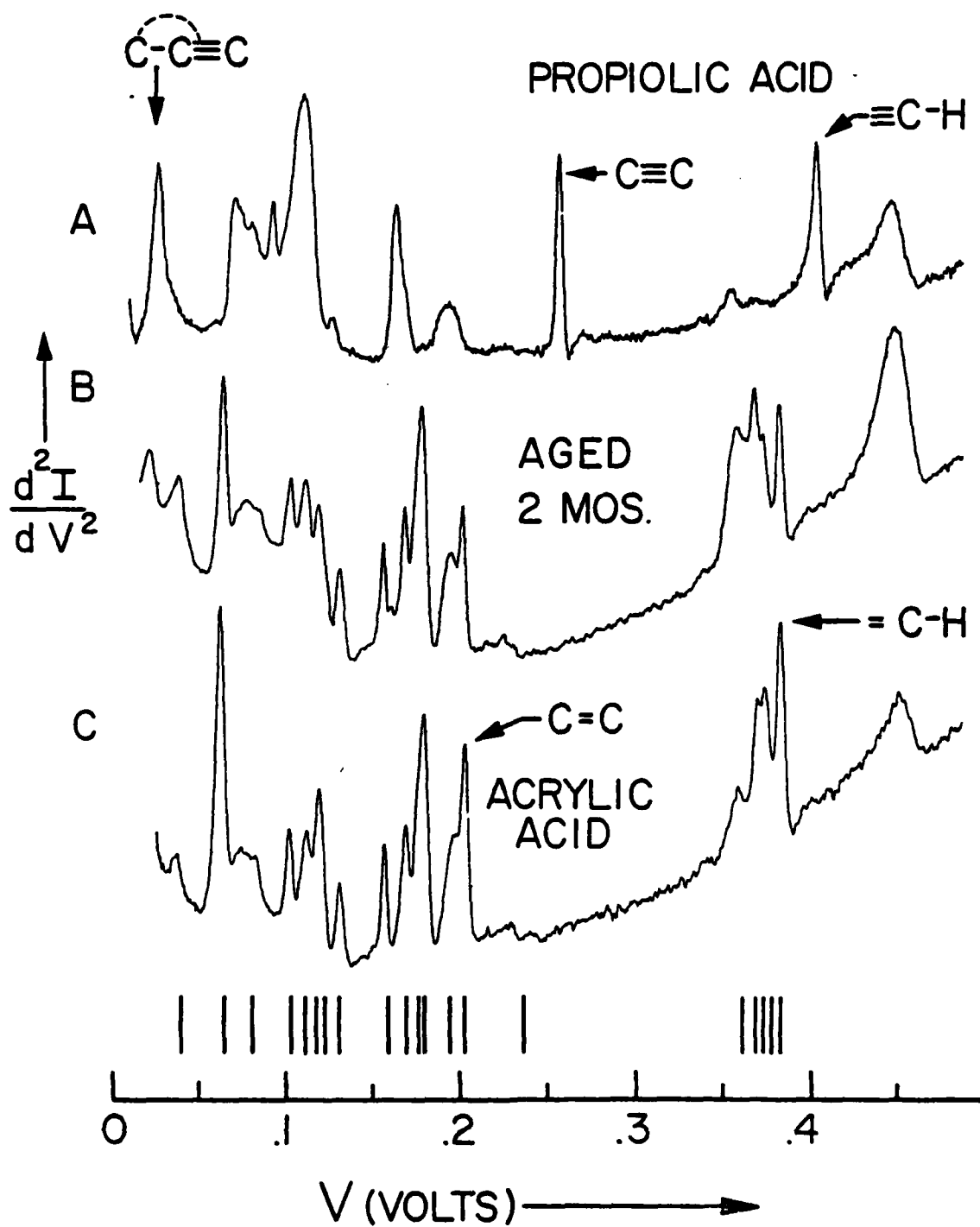


FIGURE 10

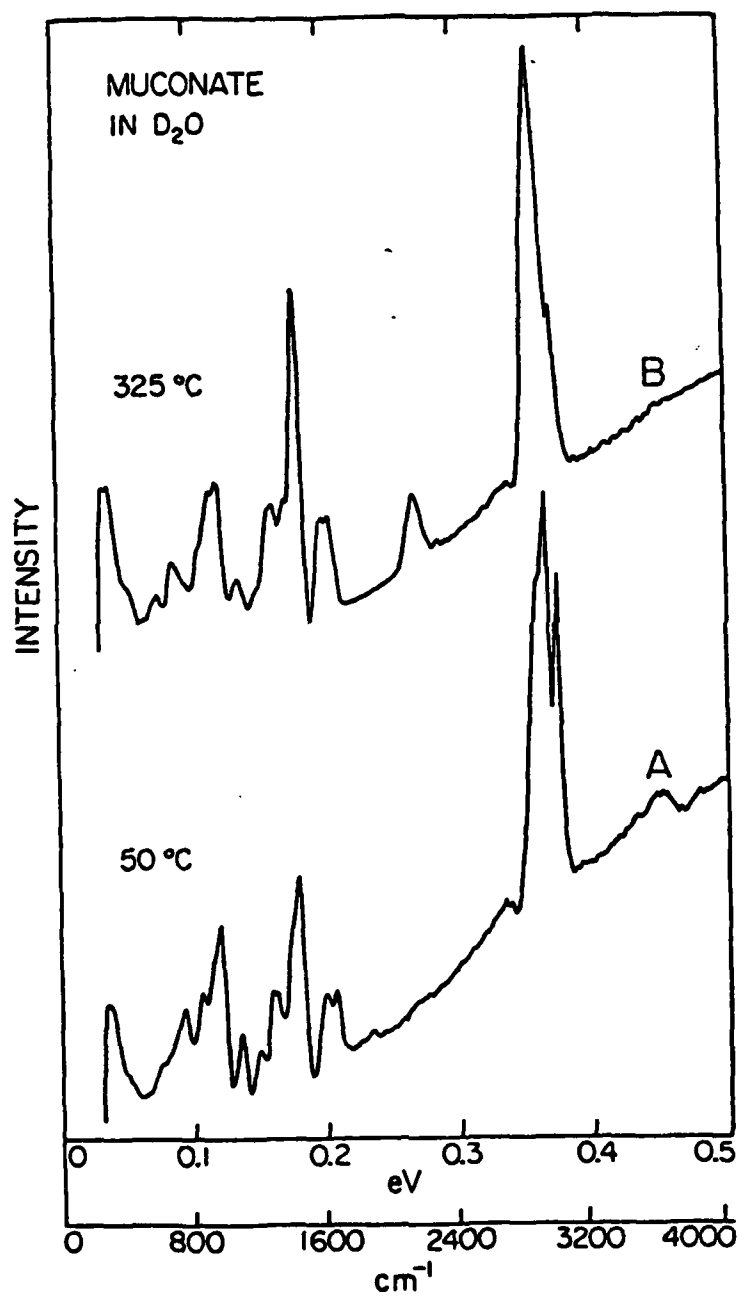


FIGURE 11

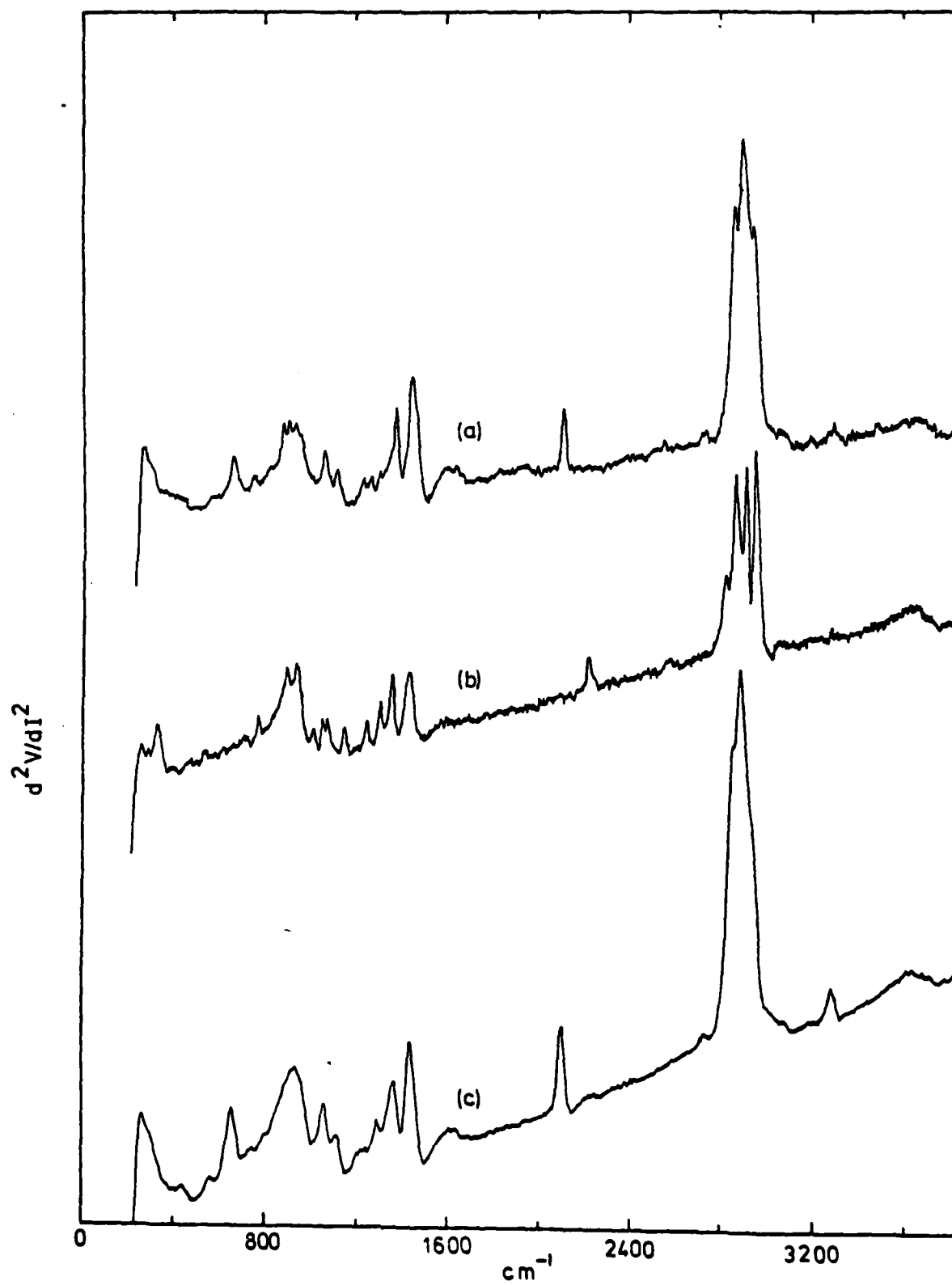


FIGURE 12

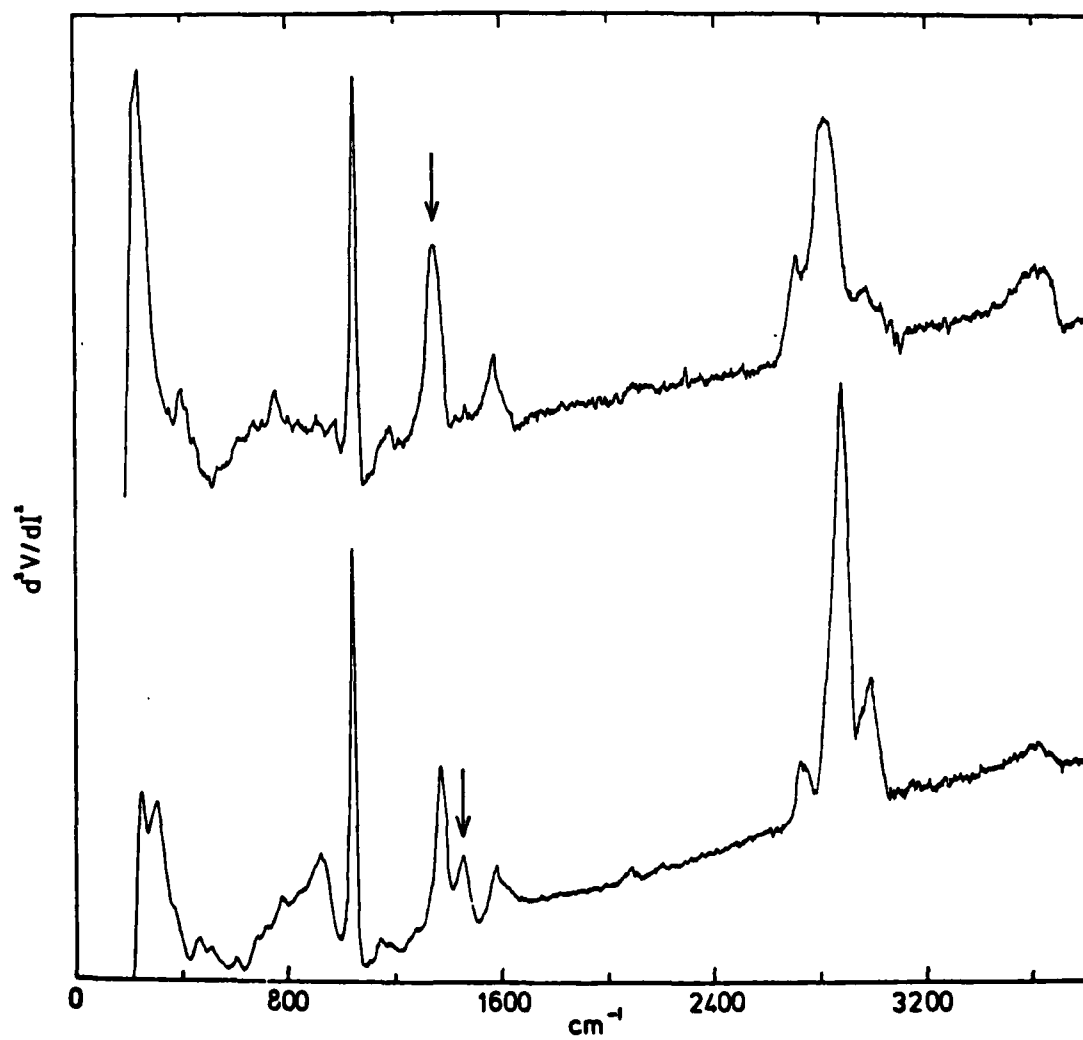


FIGURE 13

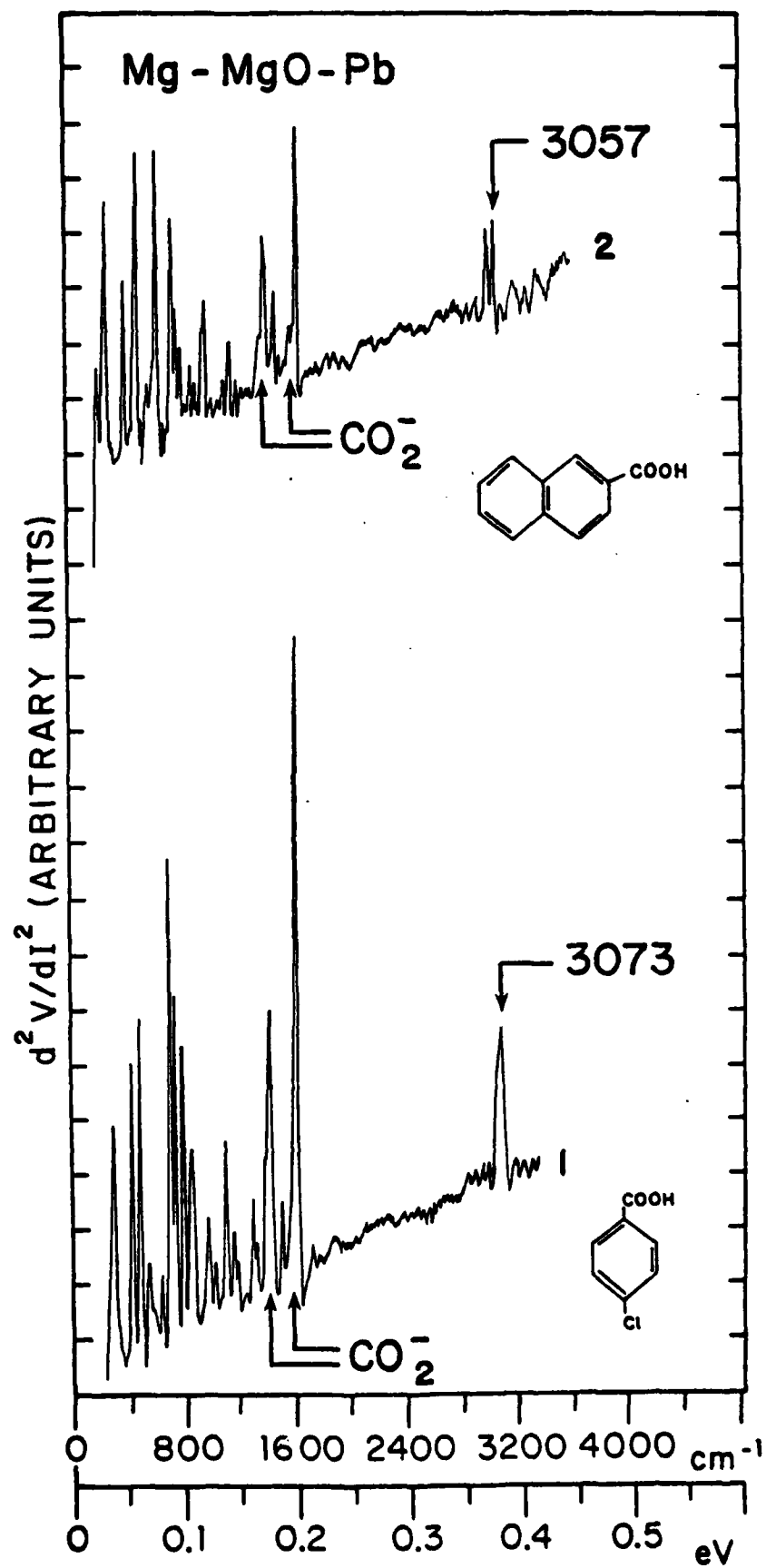
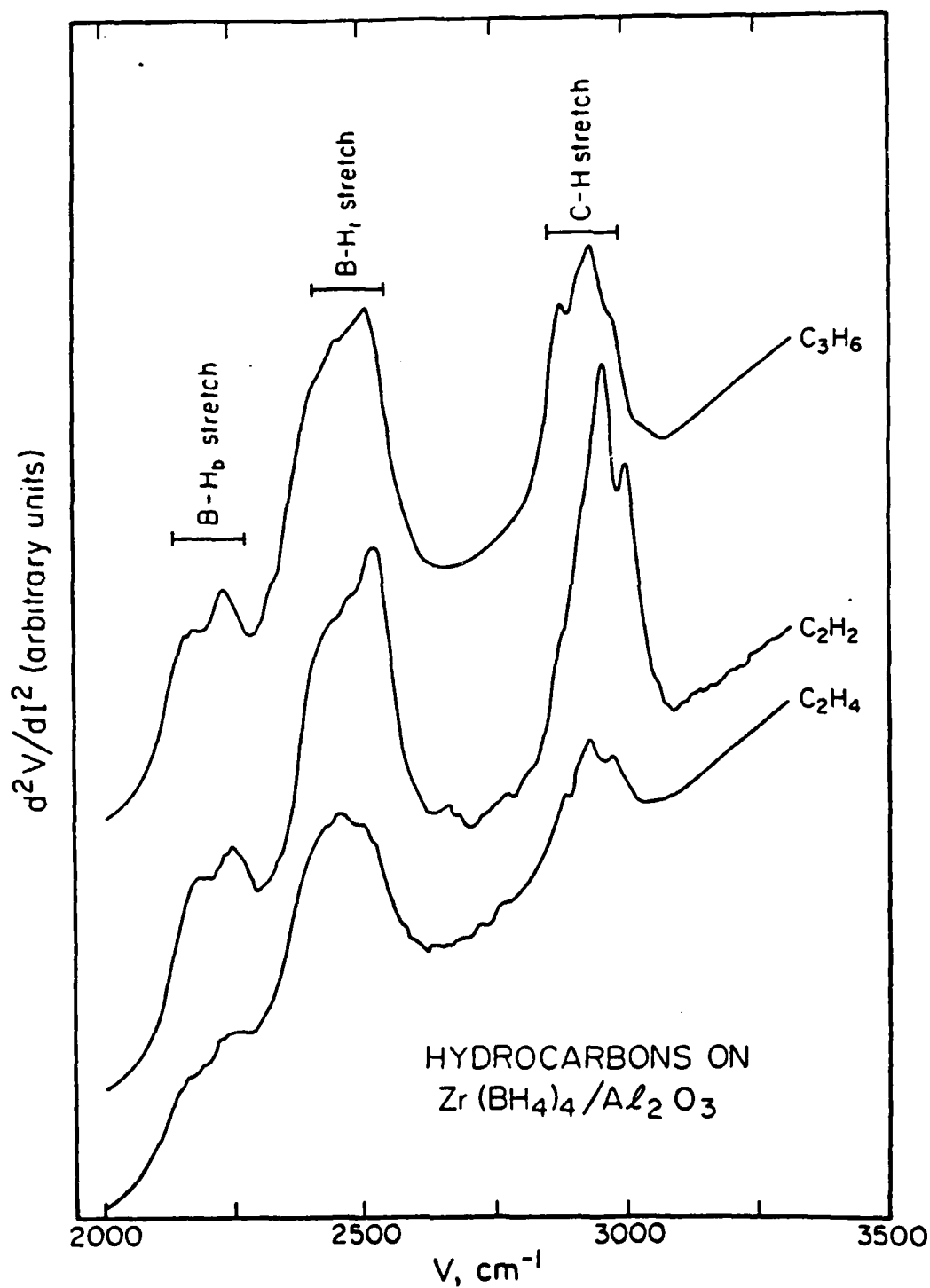




FIGURE 14



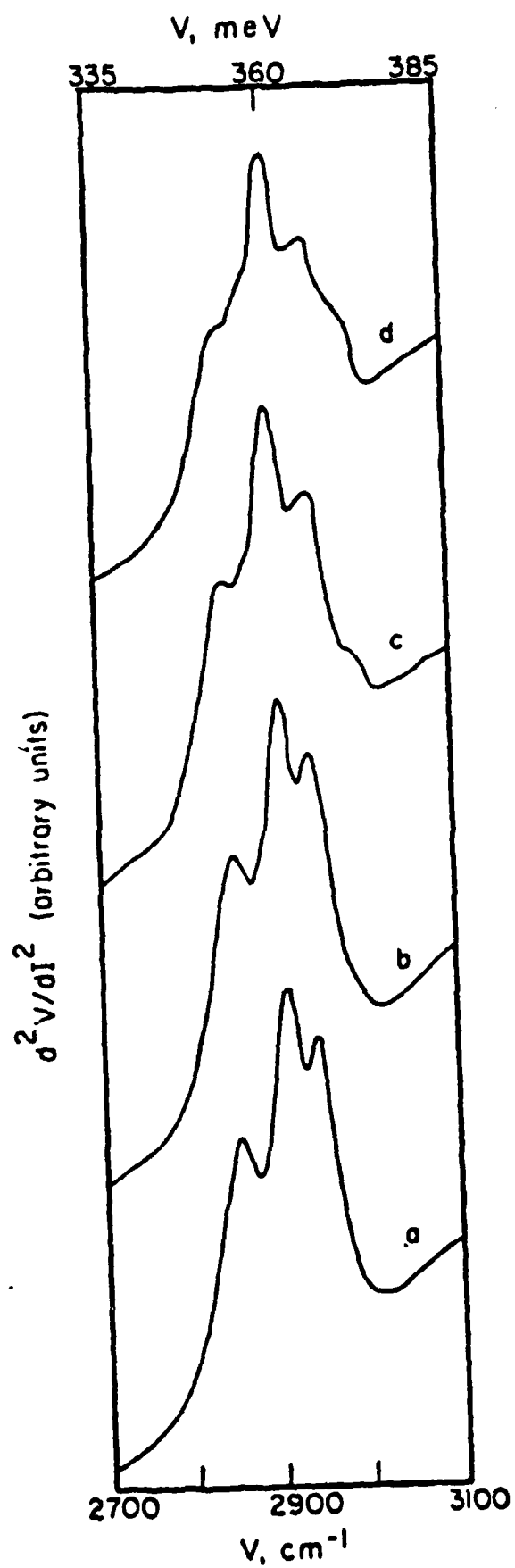
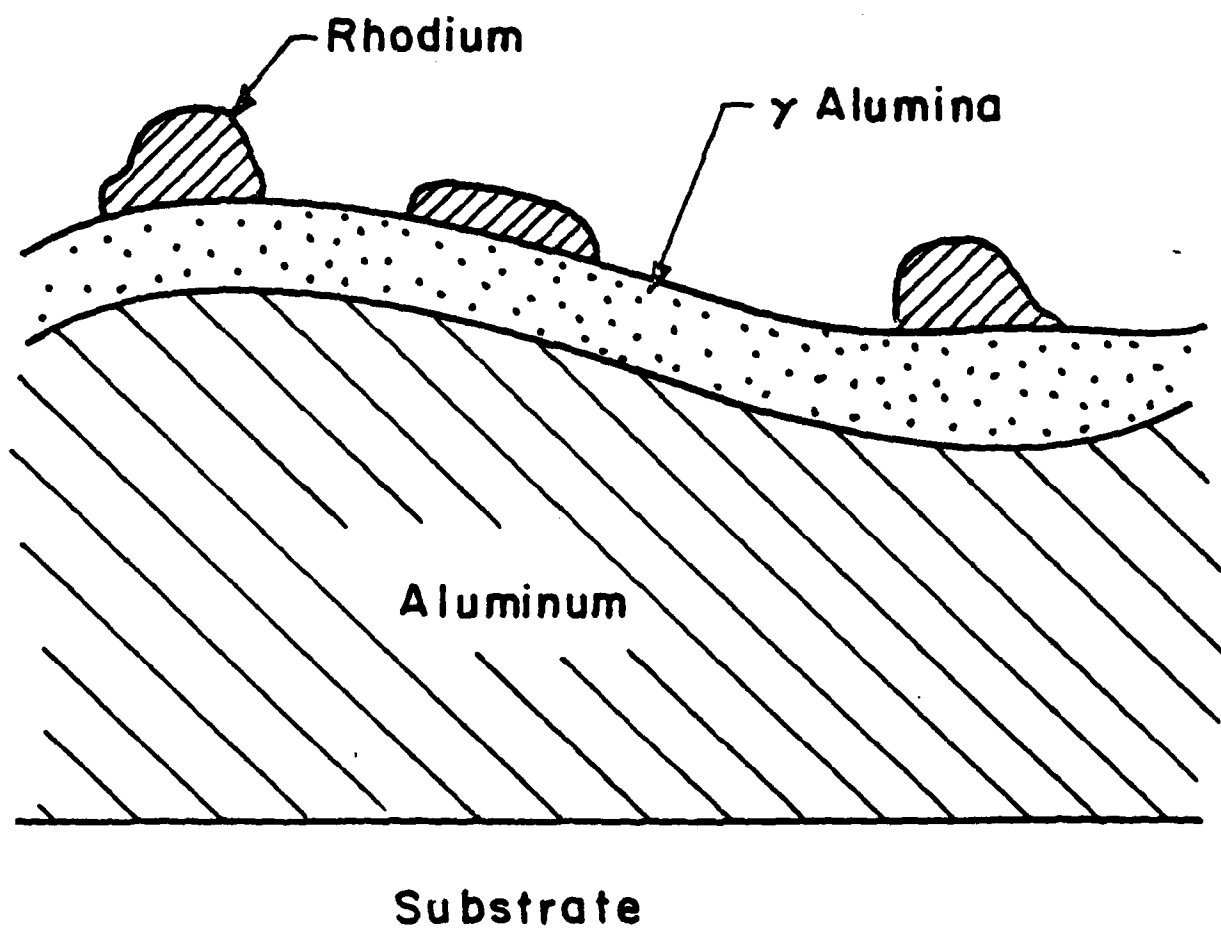


FIGURE 15

FIGURE 16

# Model Supported Rhodium Catalyst



XBL 802-4730

FIGURE 17

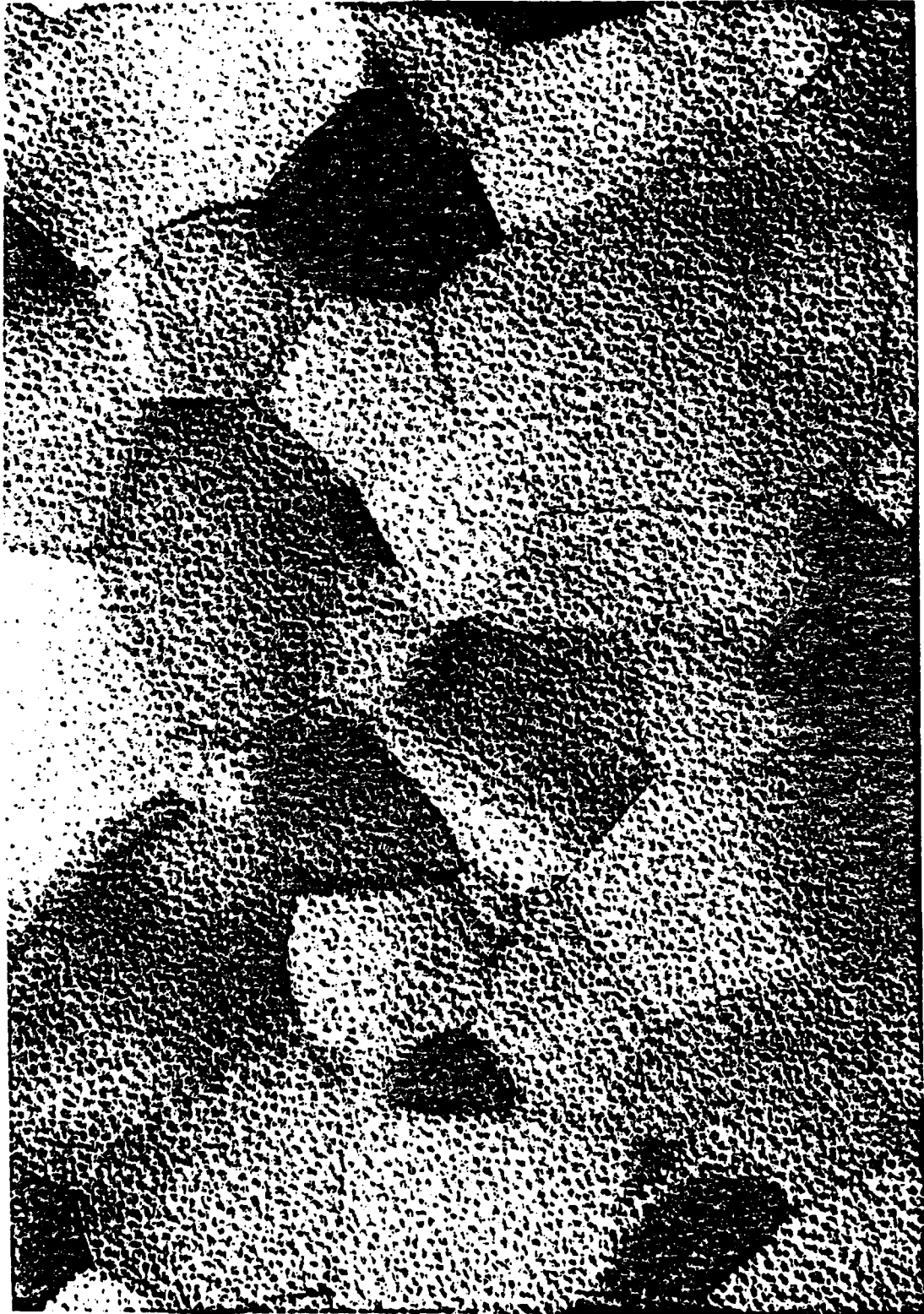
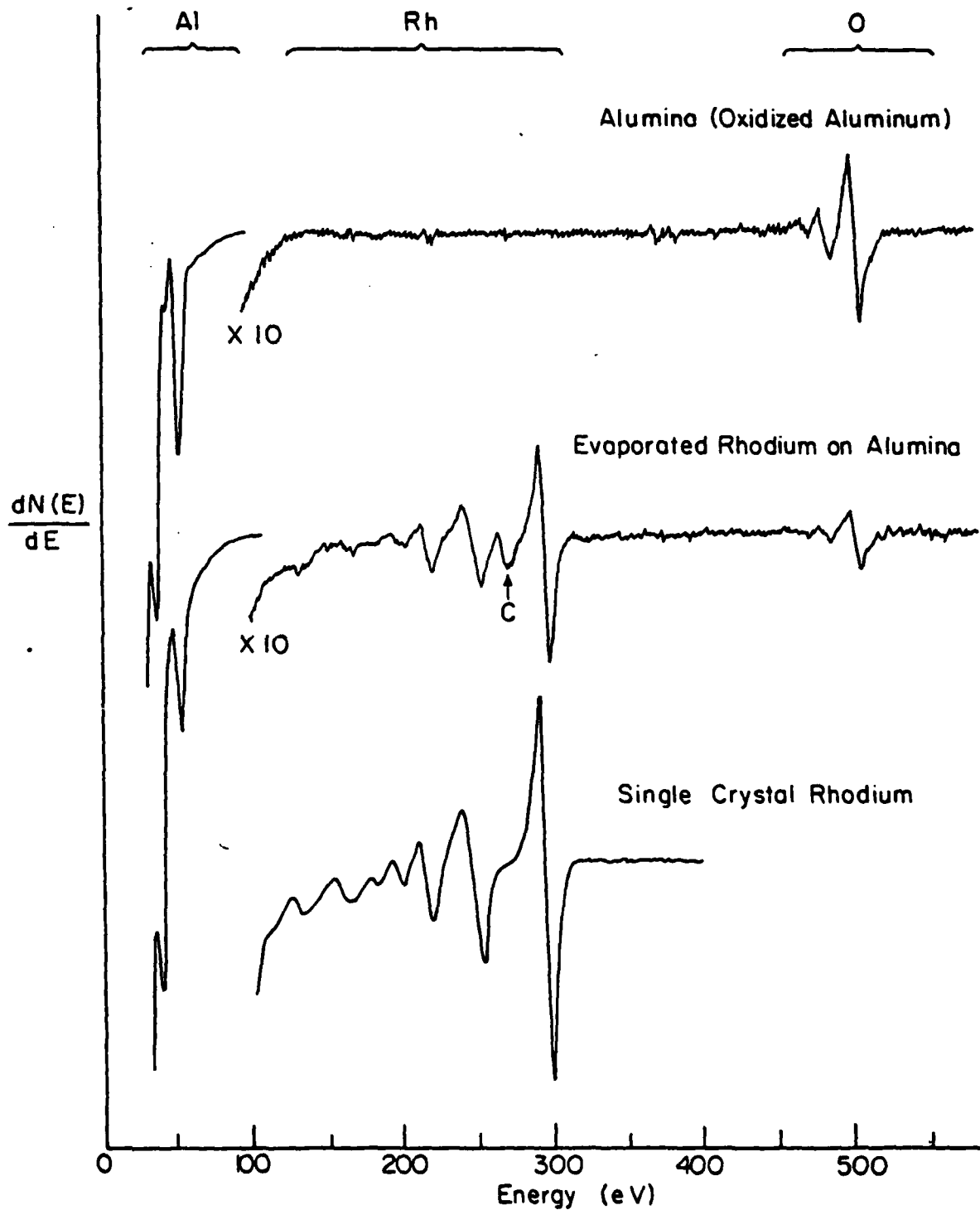


FIGURE 18

Auger Electron Spectra of Model Catalysts



XBL 802-4731

FIGURE 19

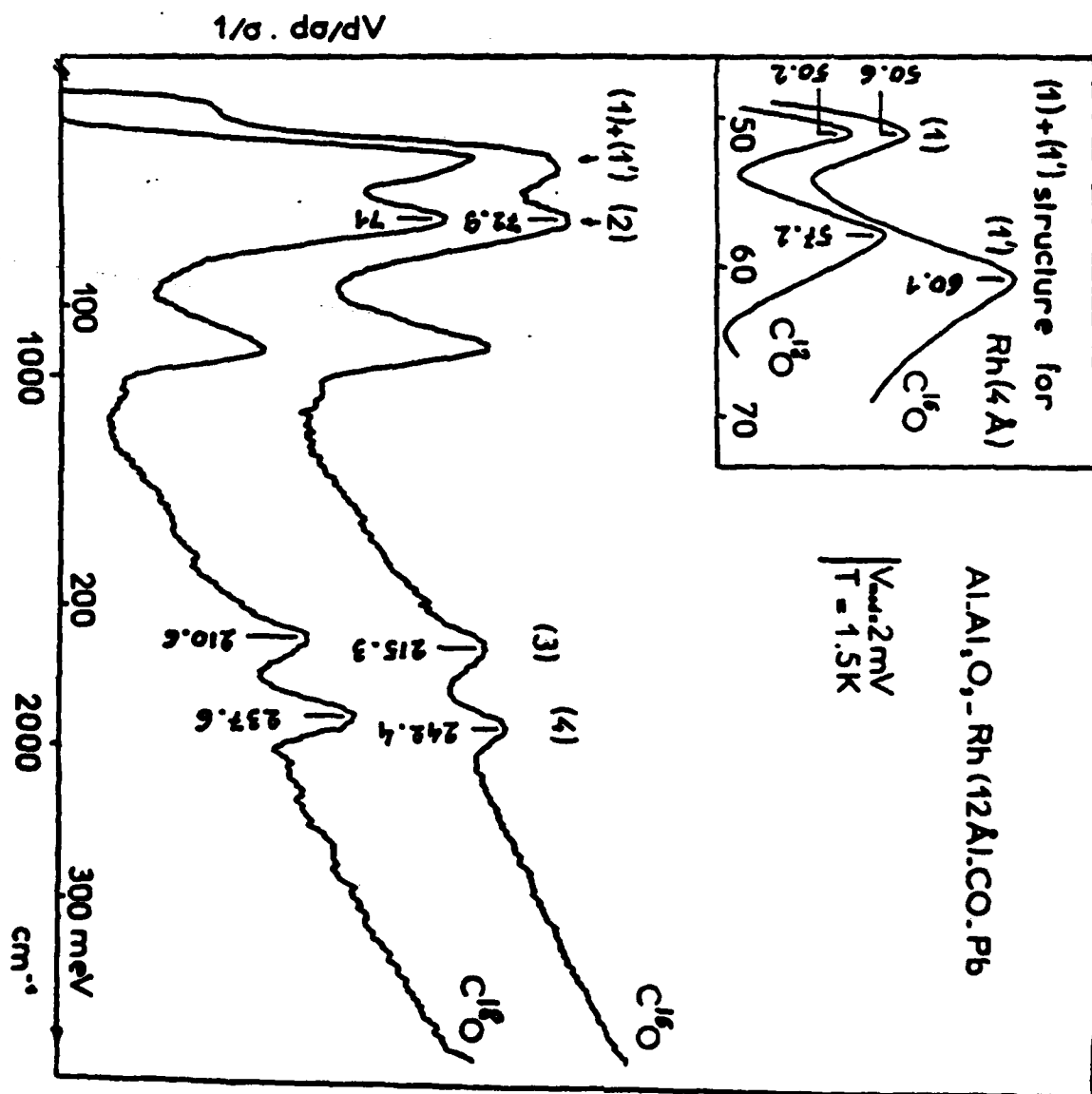


FIGURE 20

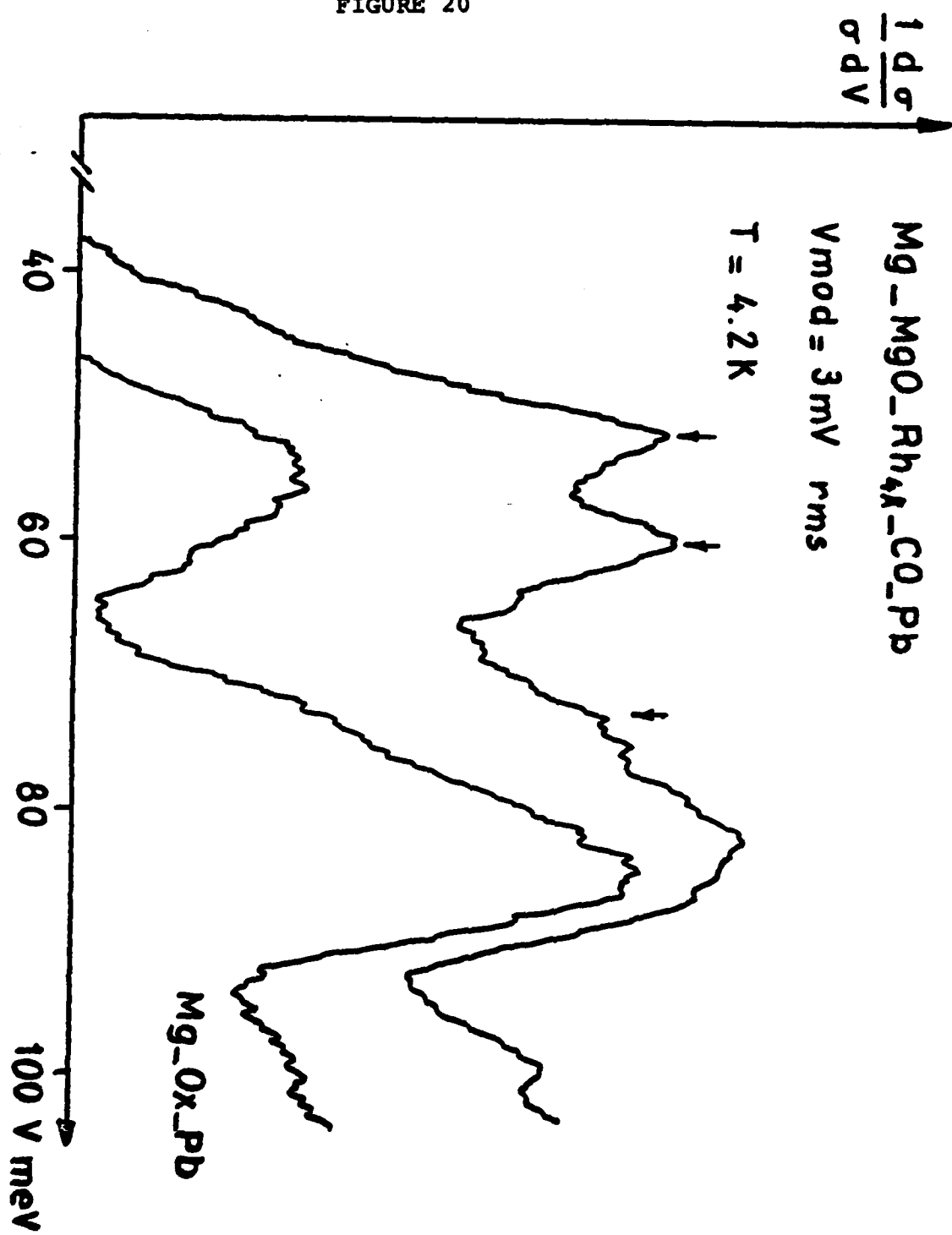


FIGURE 21

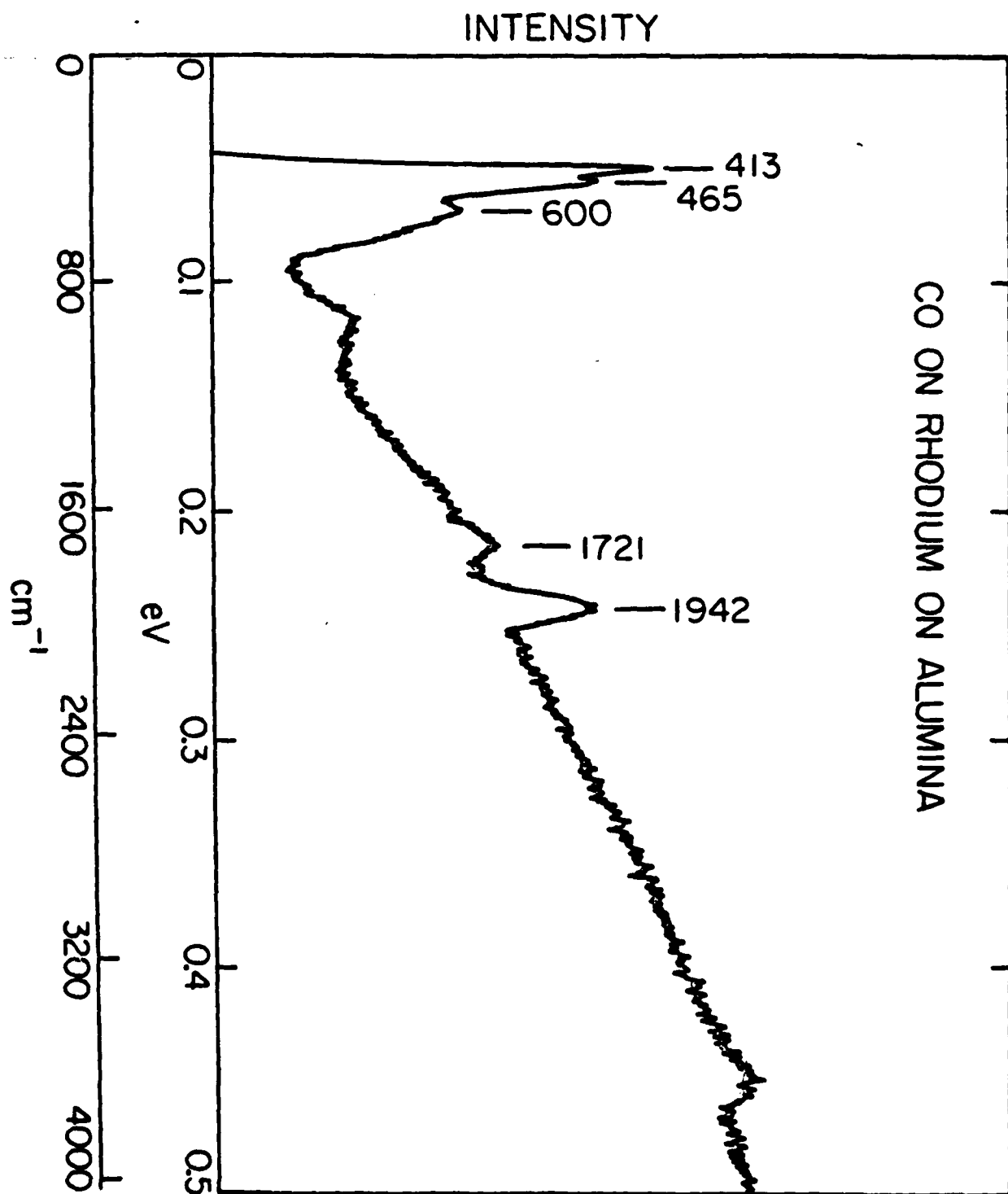




FIGURE 22

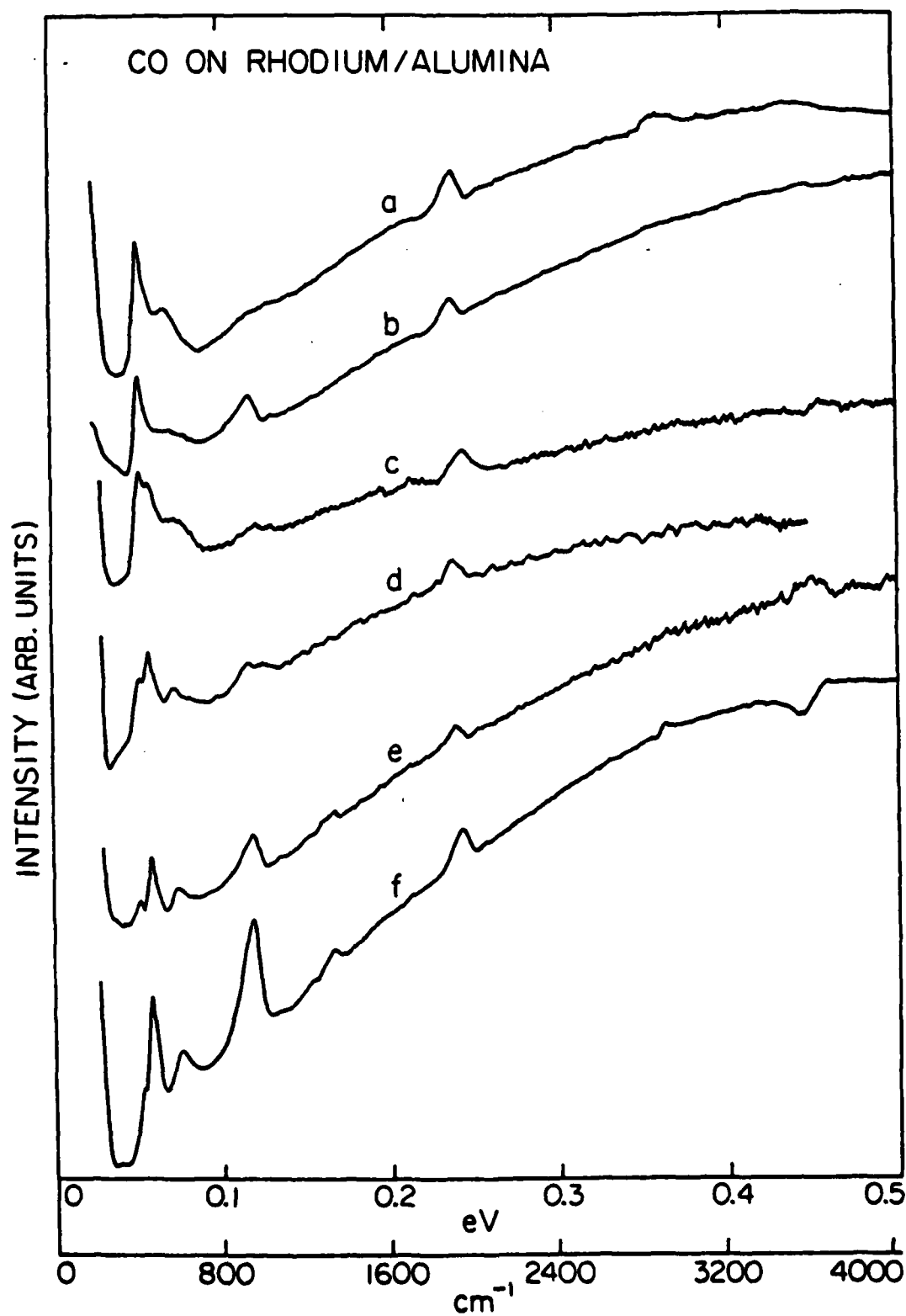


FIGURE 23

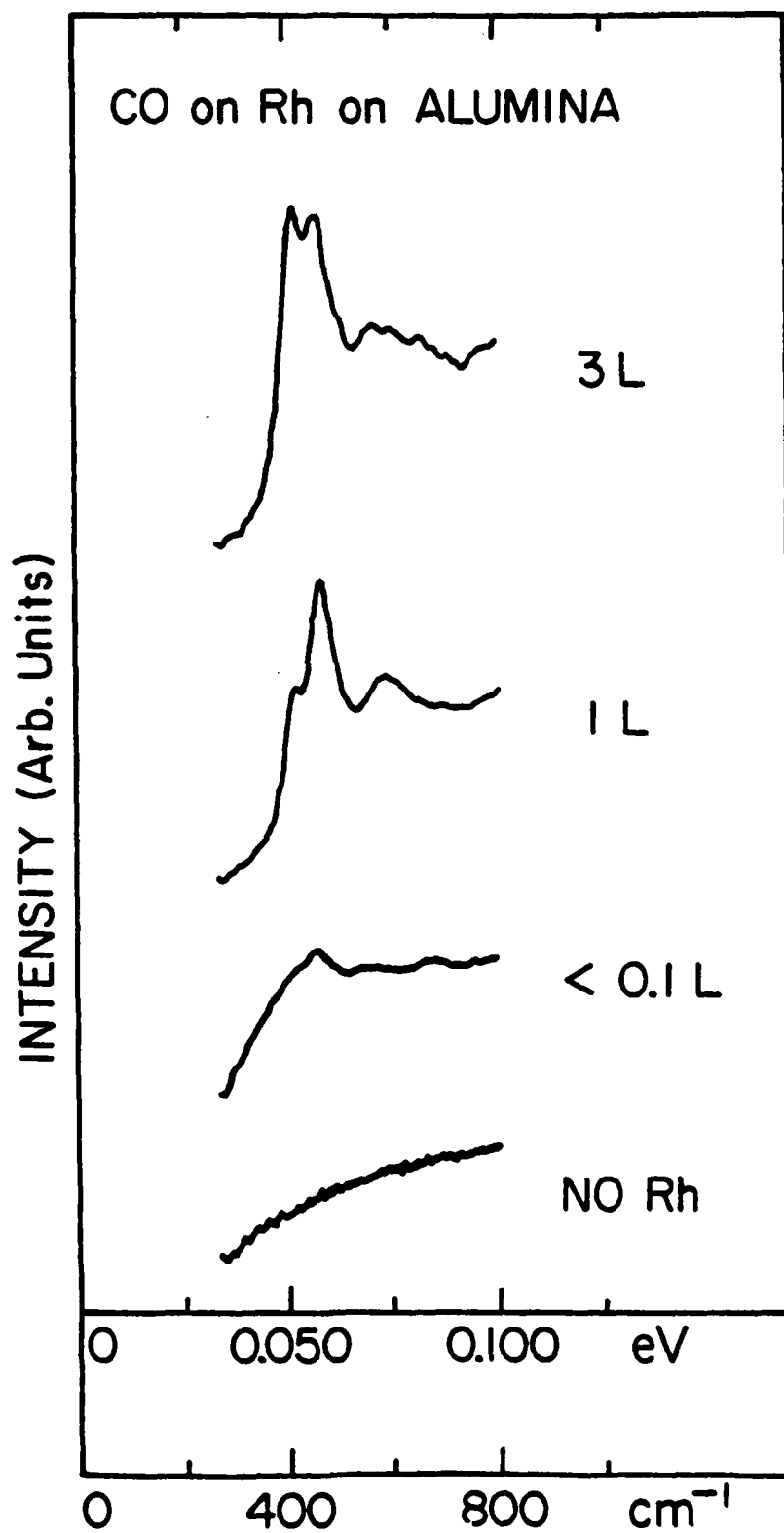


FIGURE 24

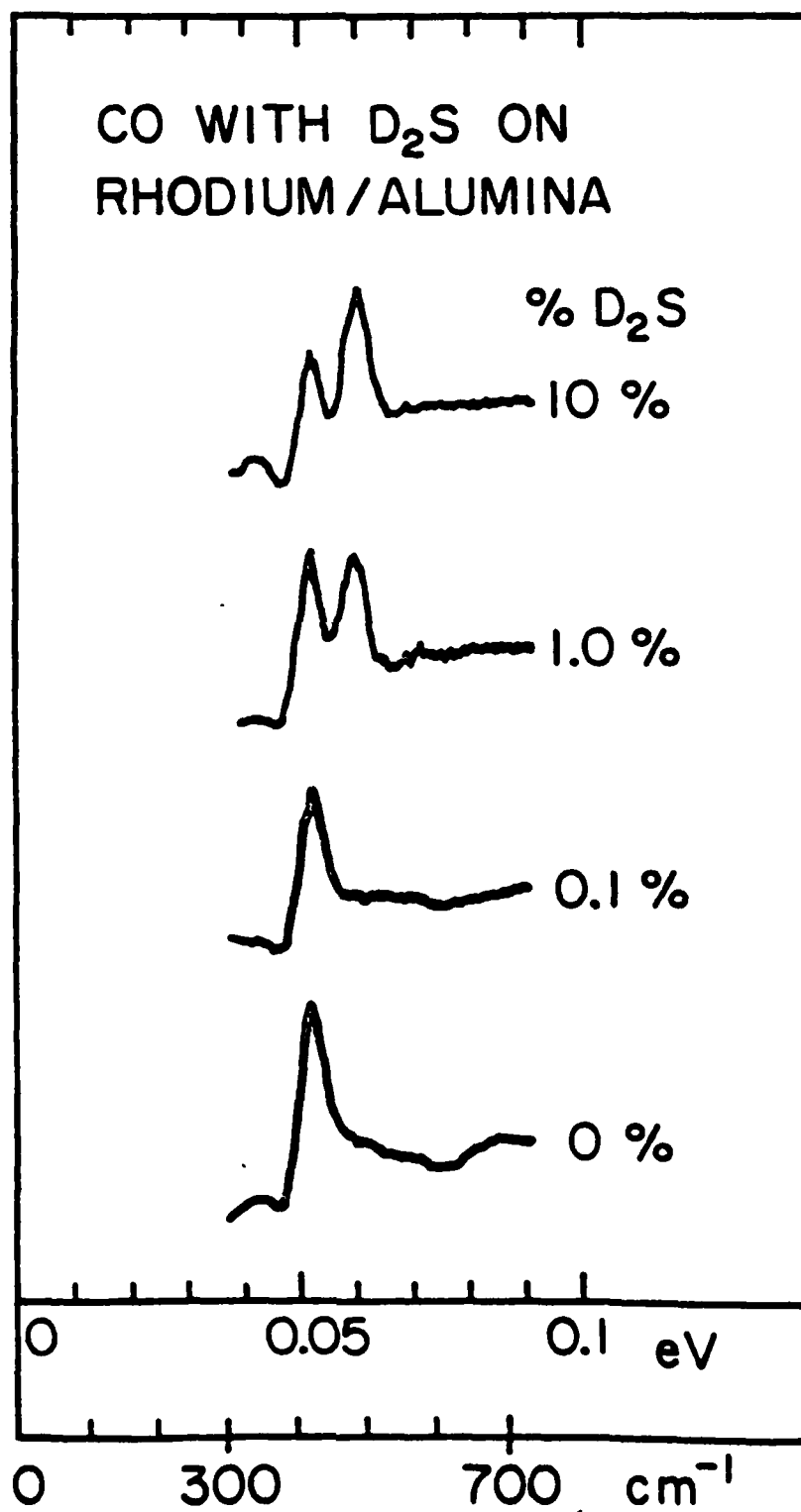


FIGURE 25

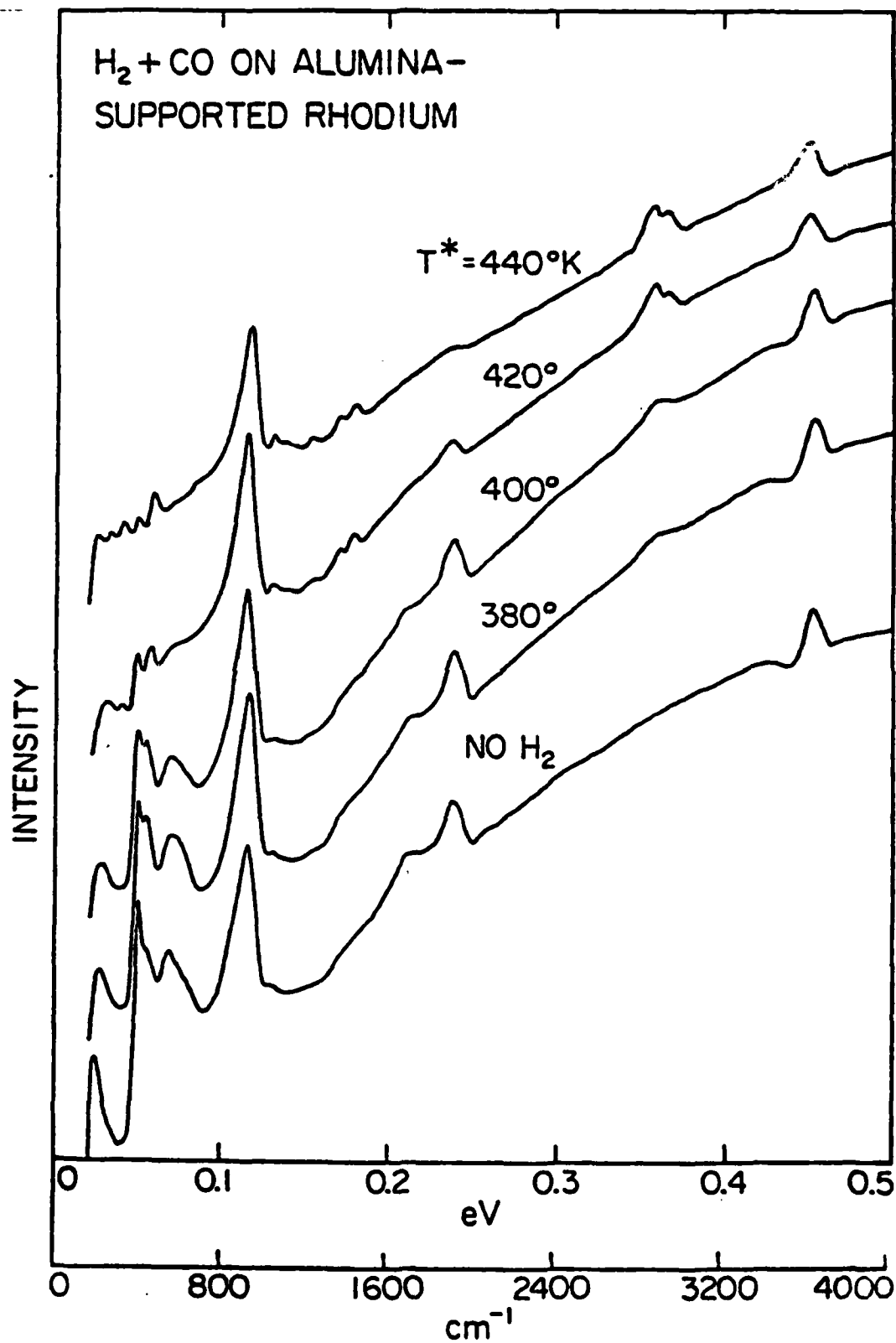


FIGURE 26

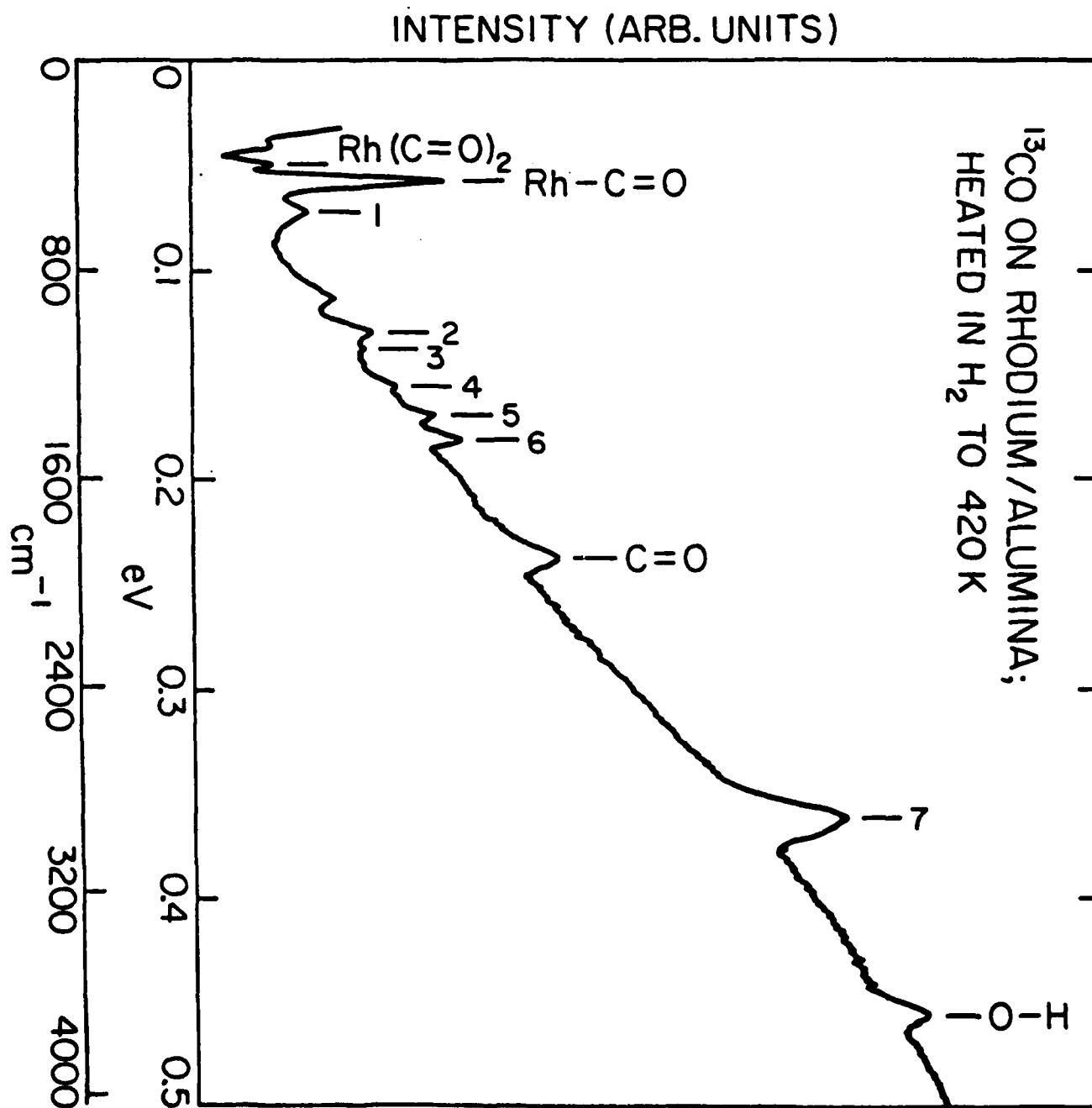


FIGURE 27

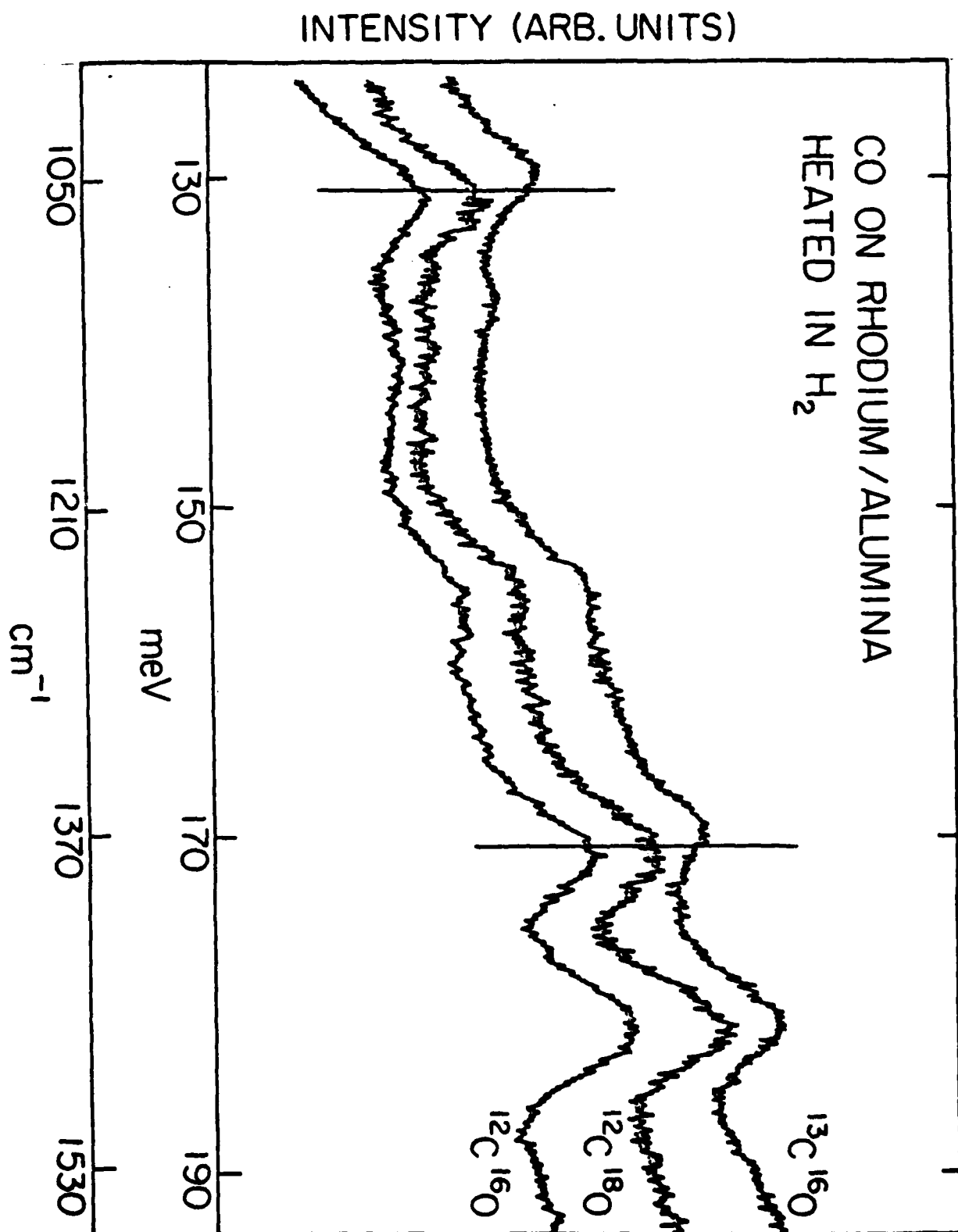


FIGURE 28

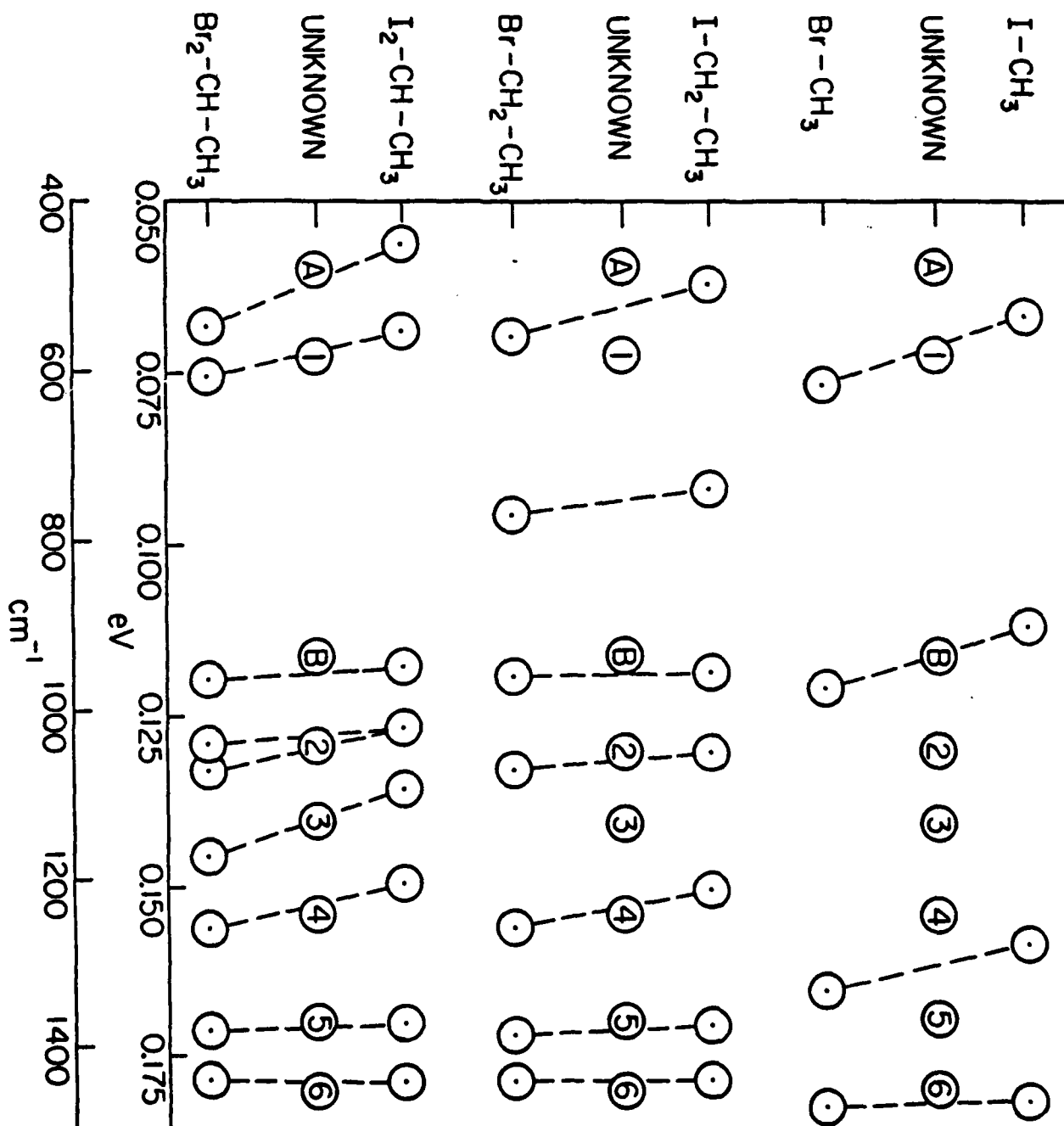


FIGURE 29

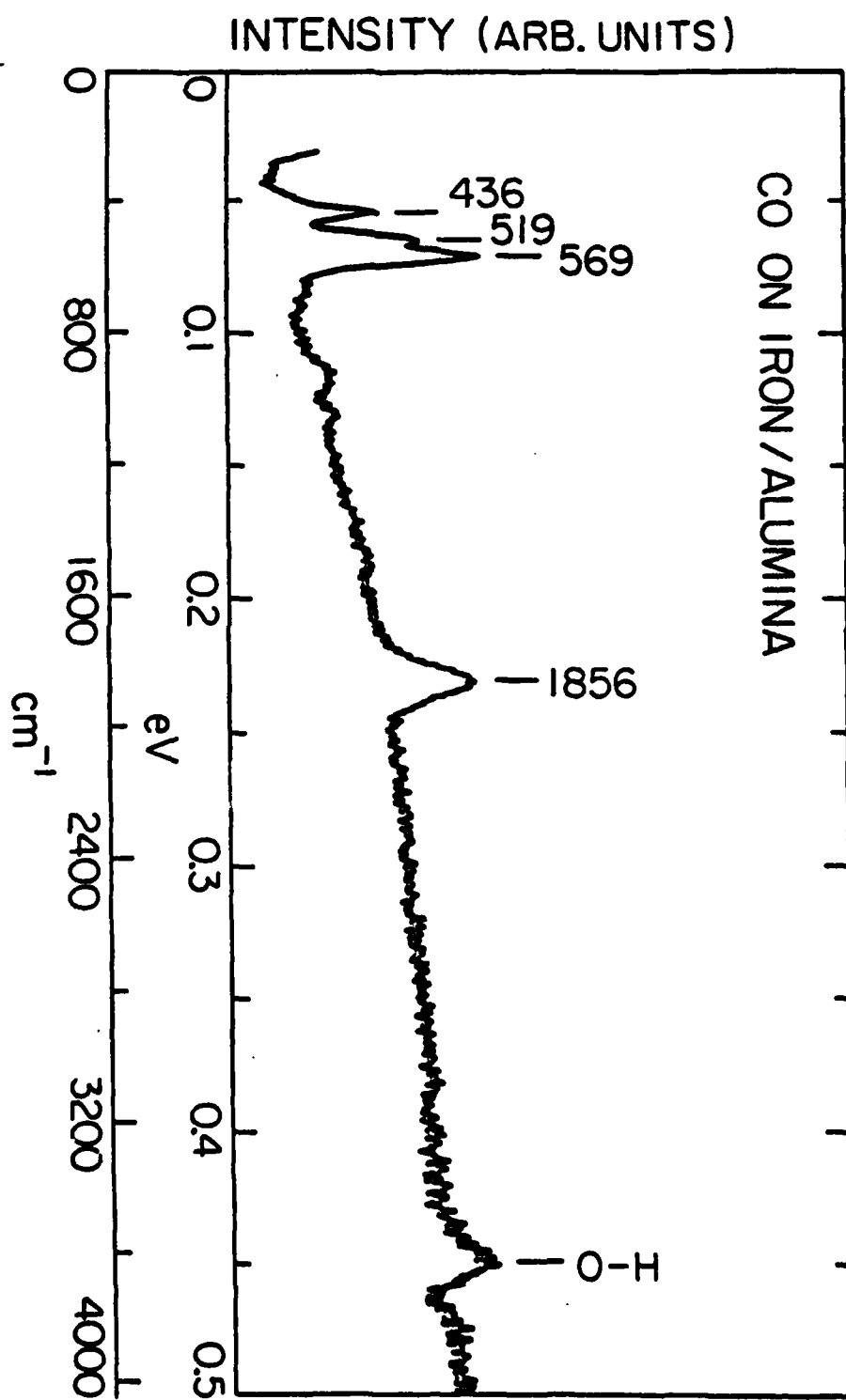




FIGURE 30

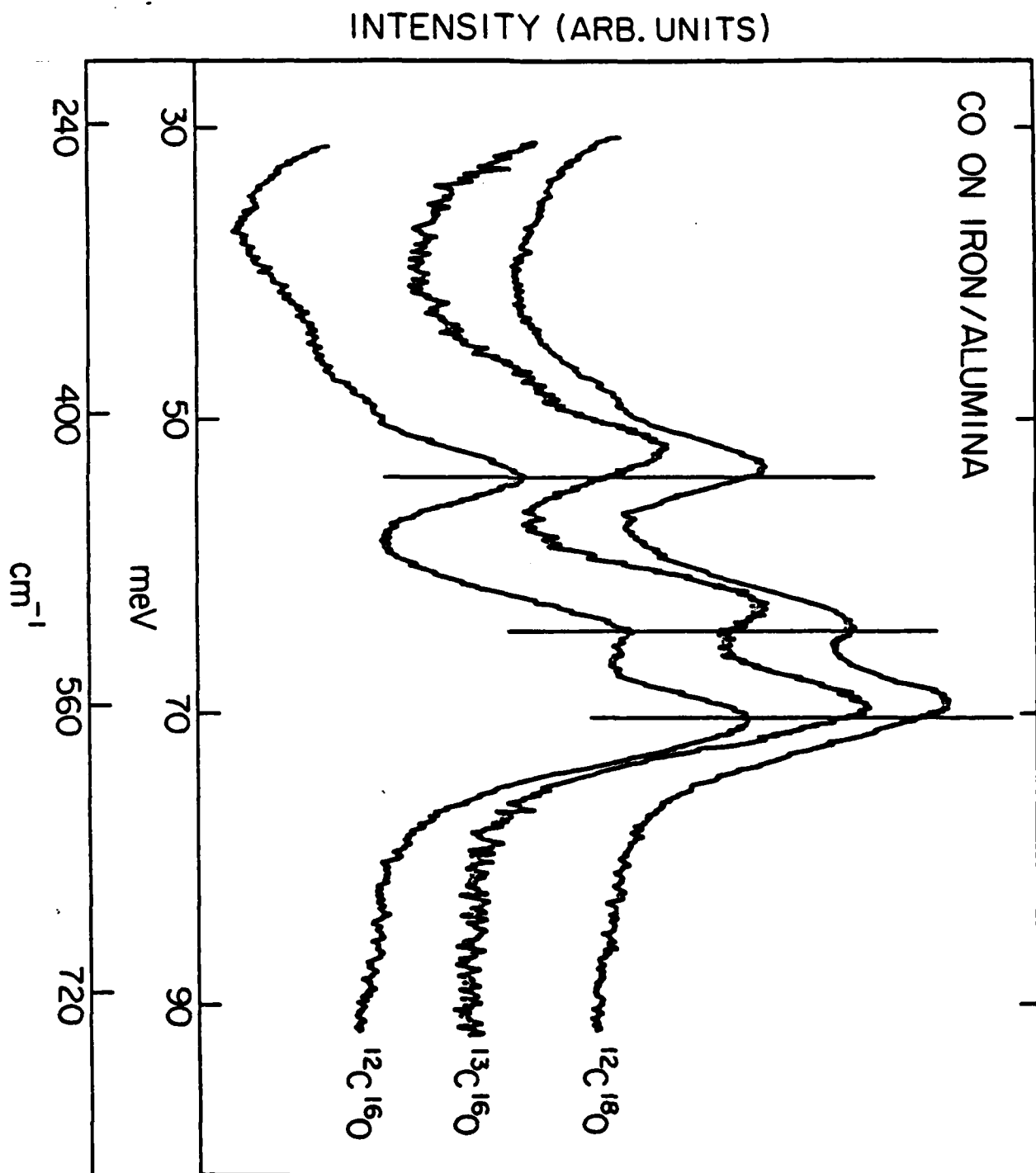


FIGURE 31

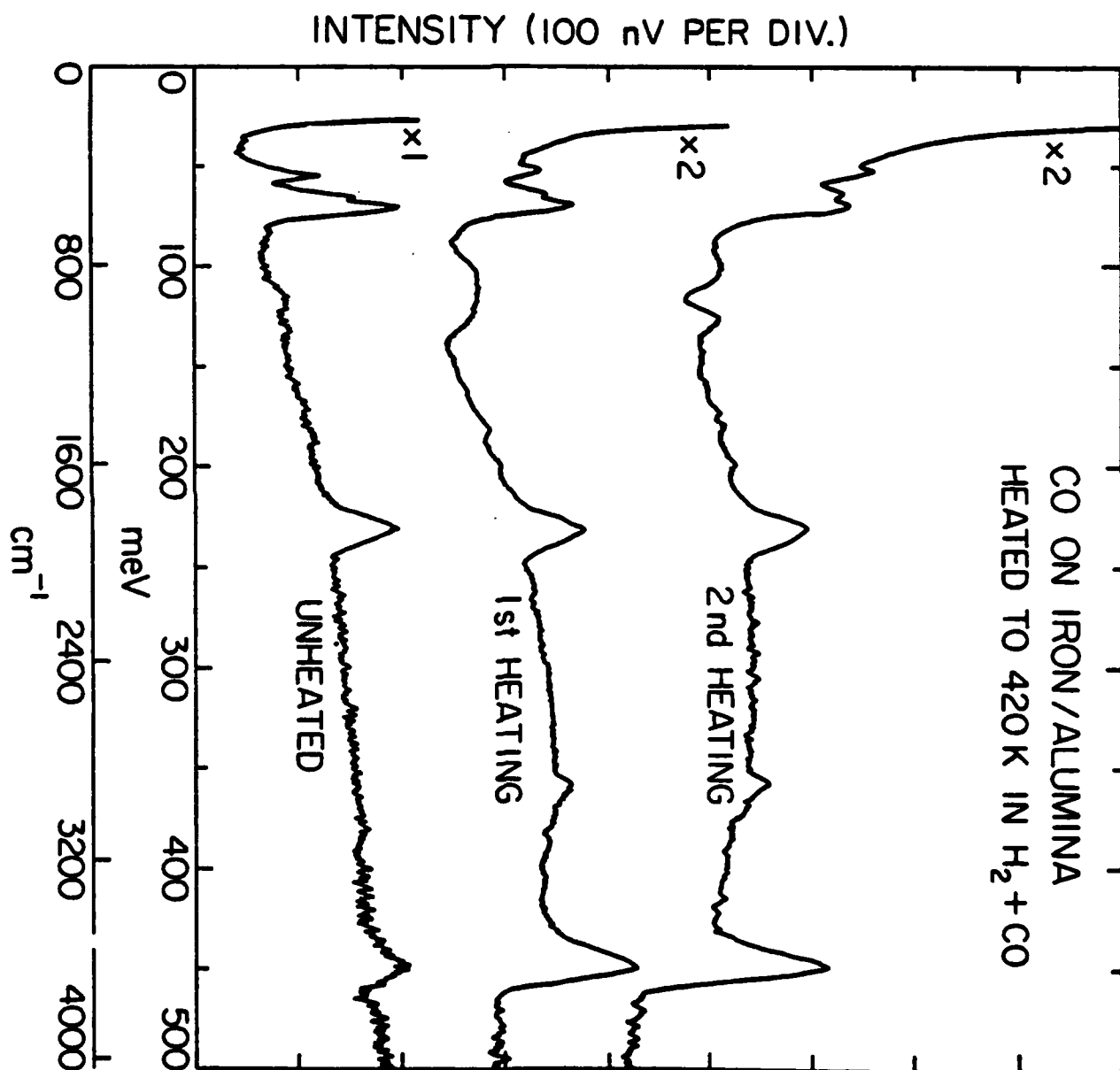


FIGURE 32

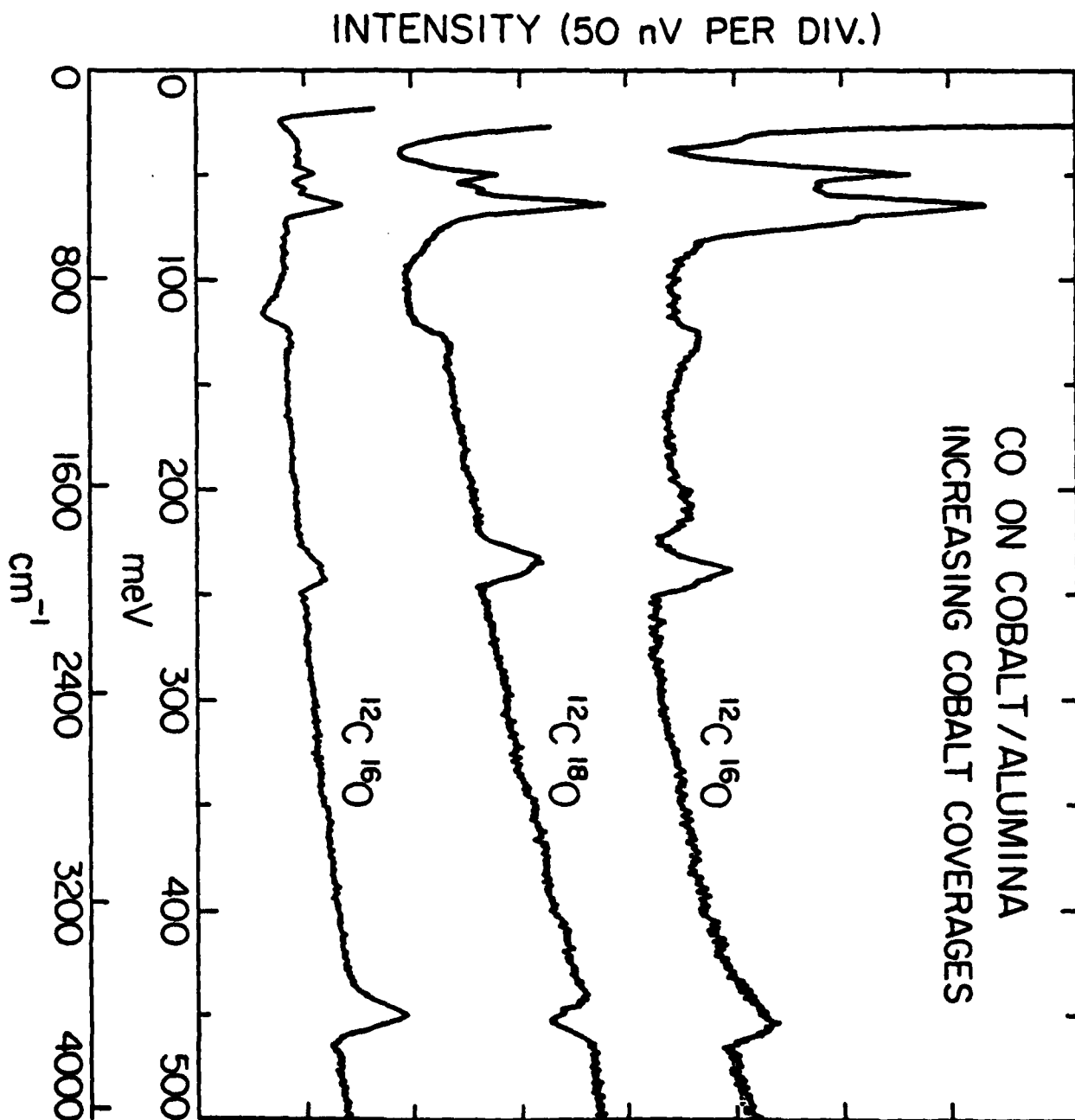


FIGURE 33

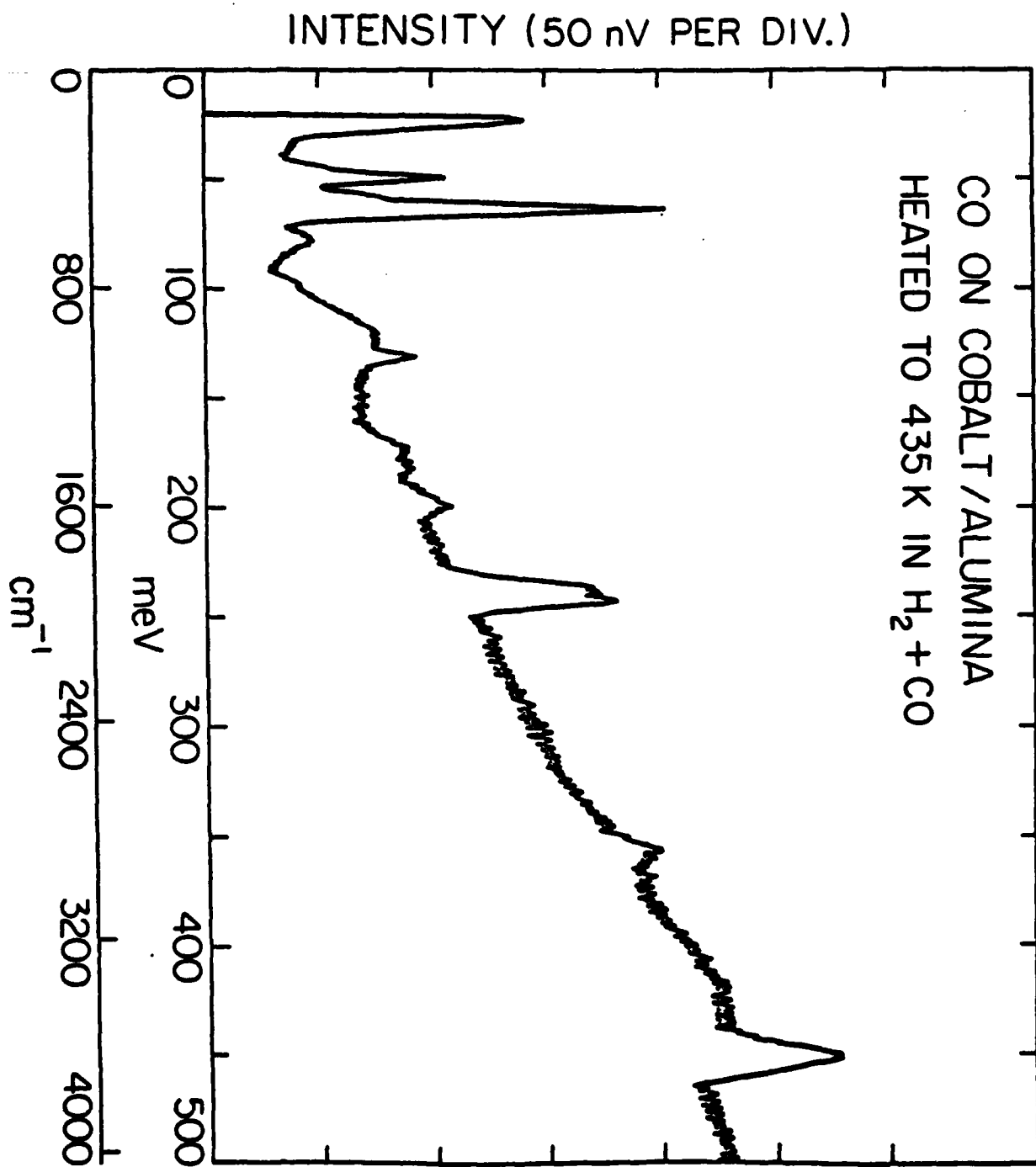


FIGURE 34

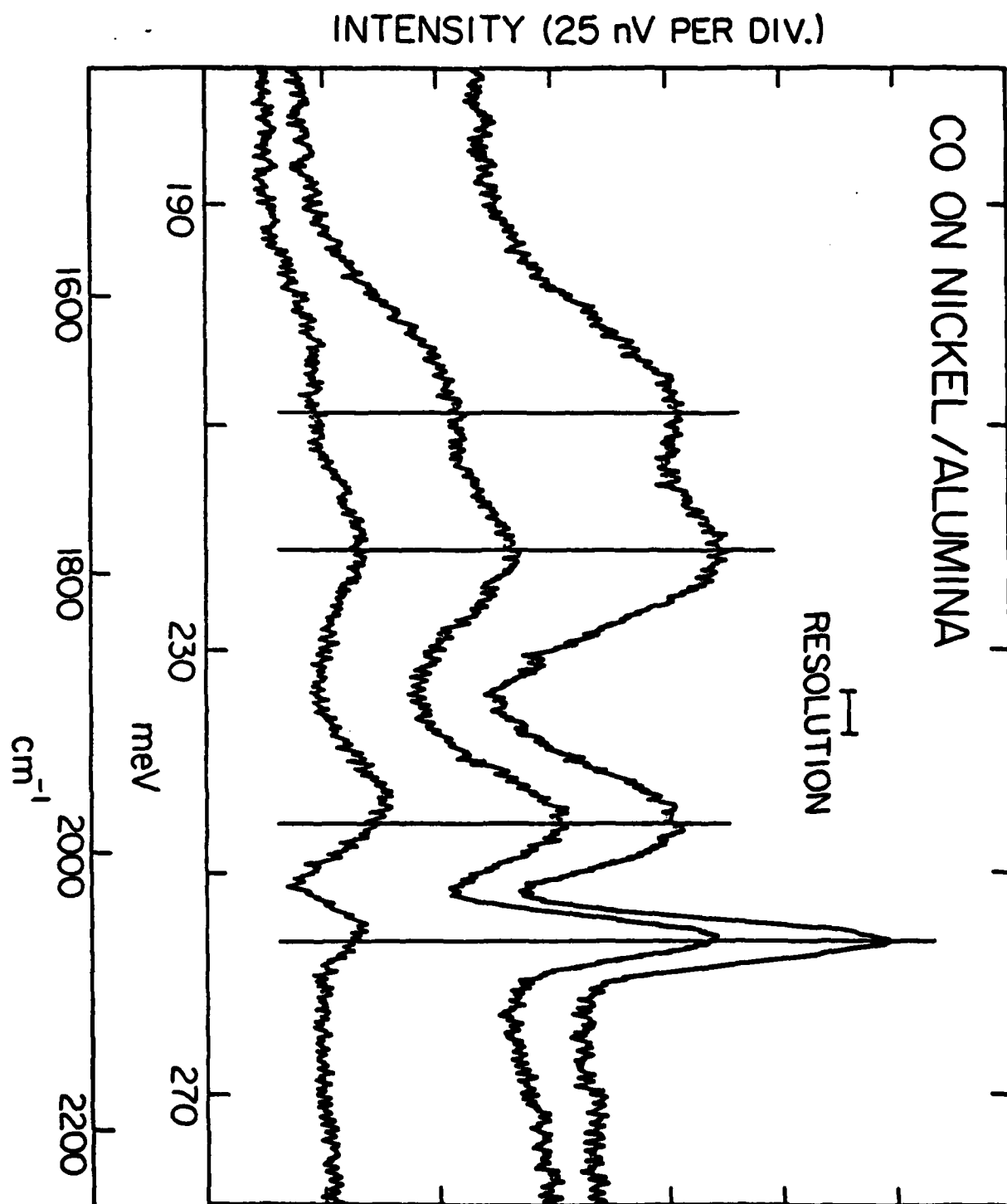


FIGURE 35

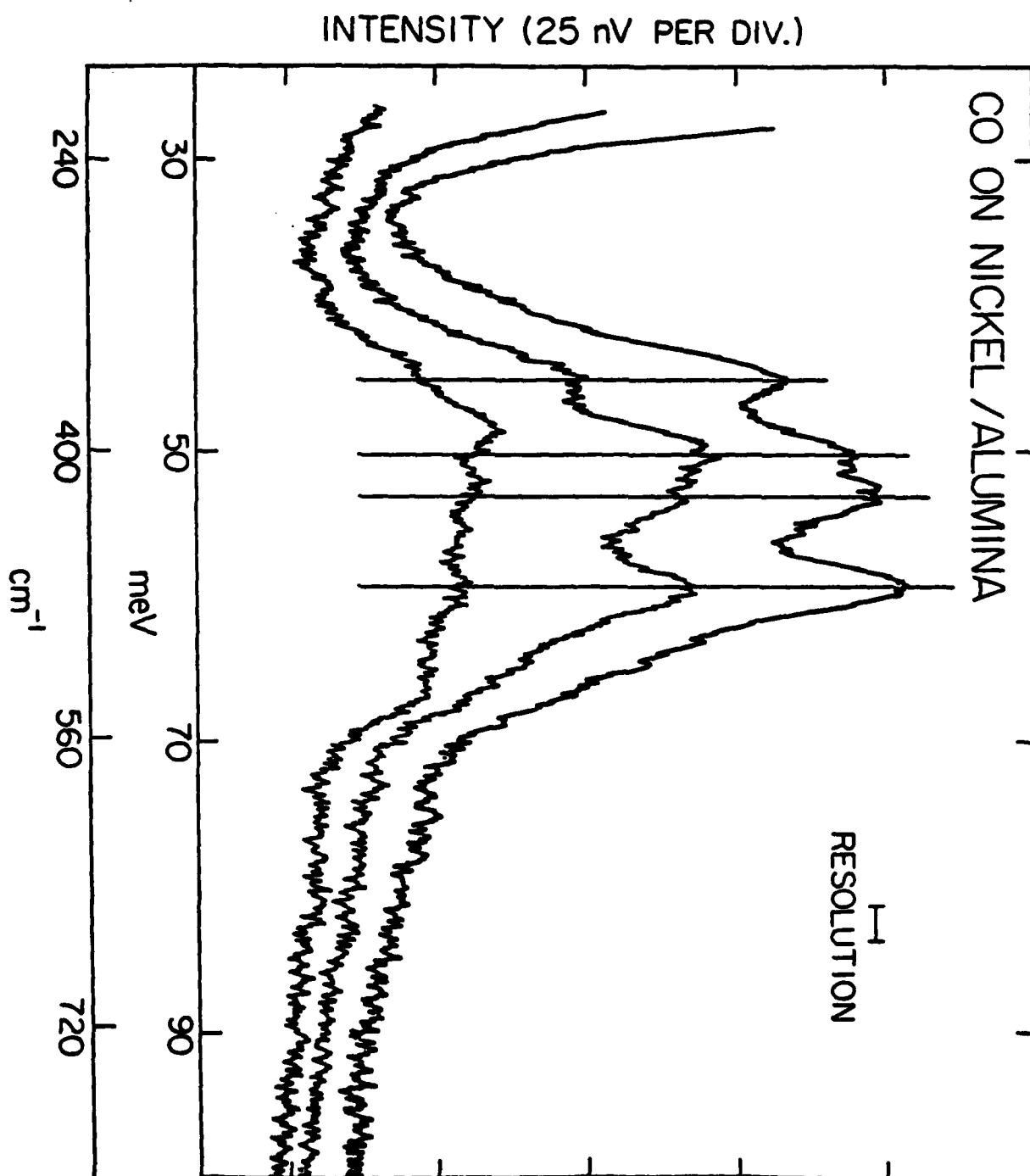


FIGURE 36

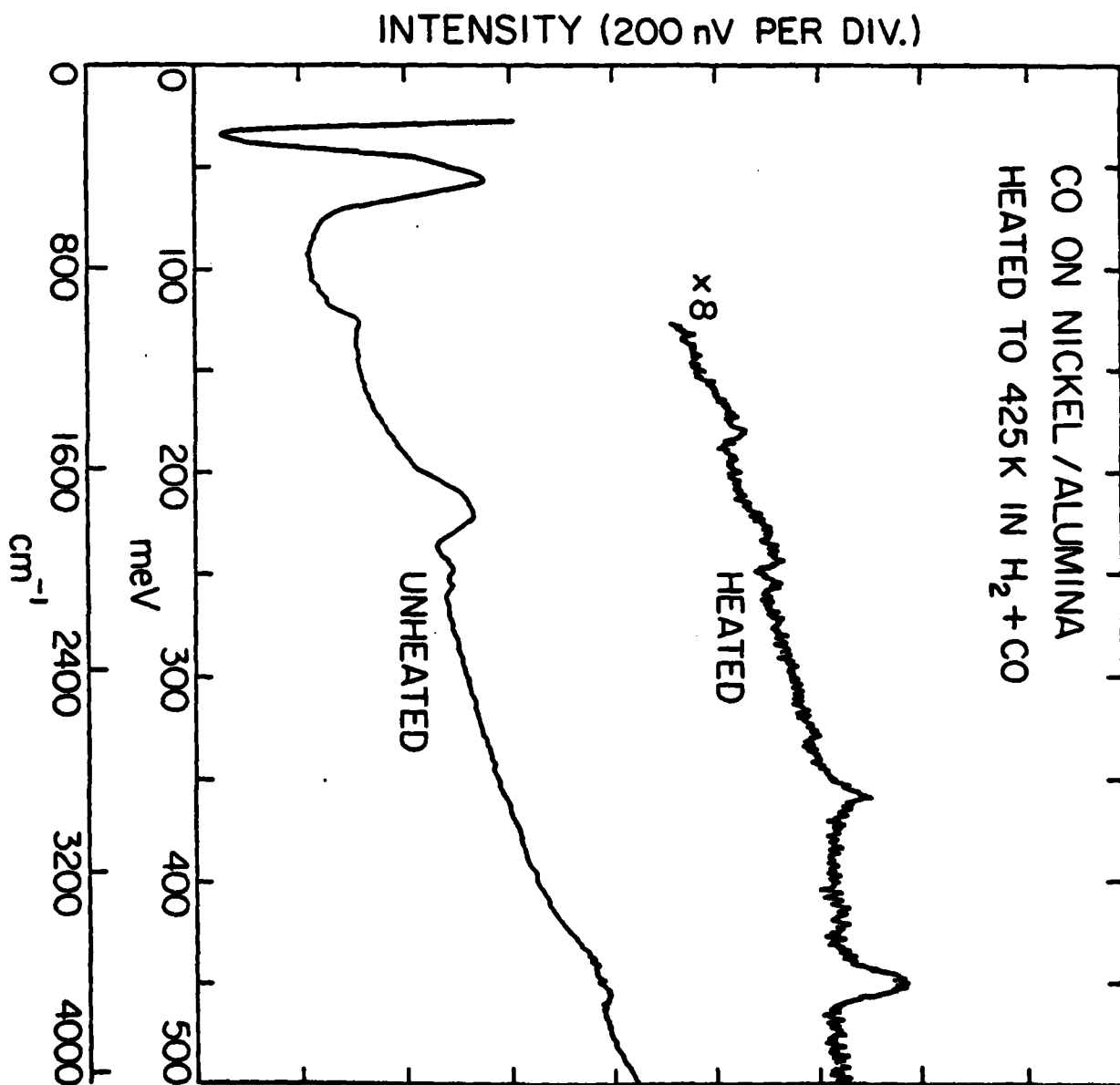
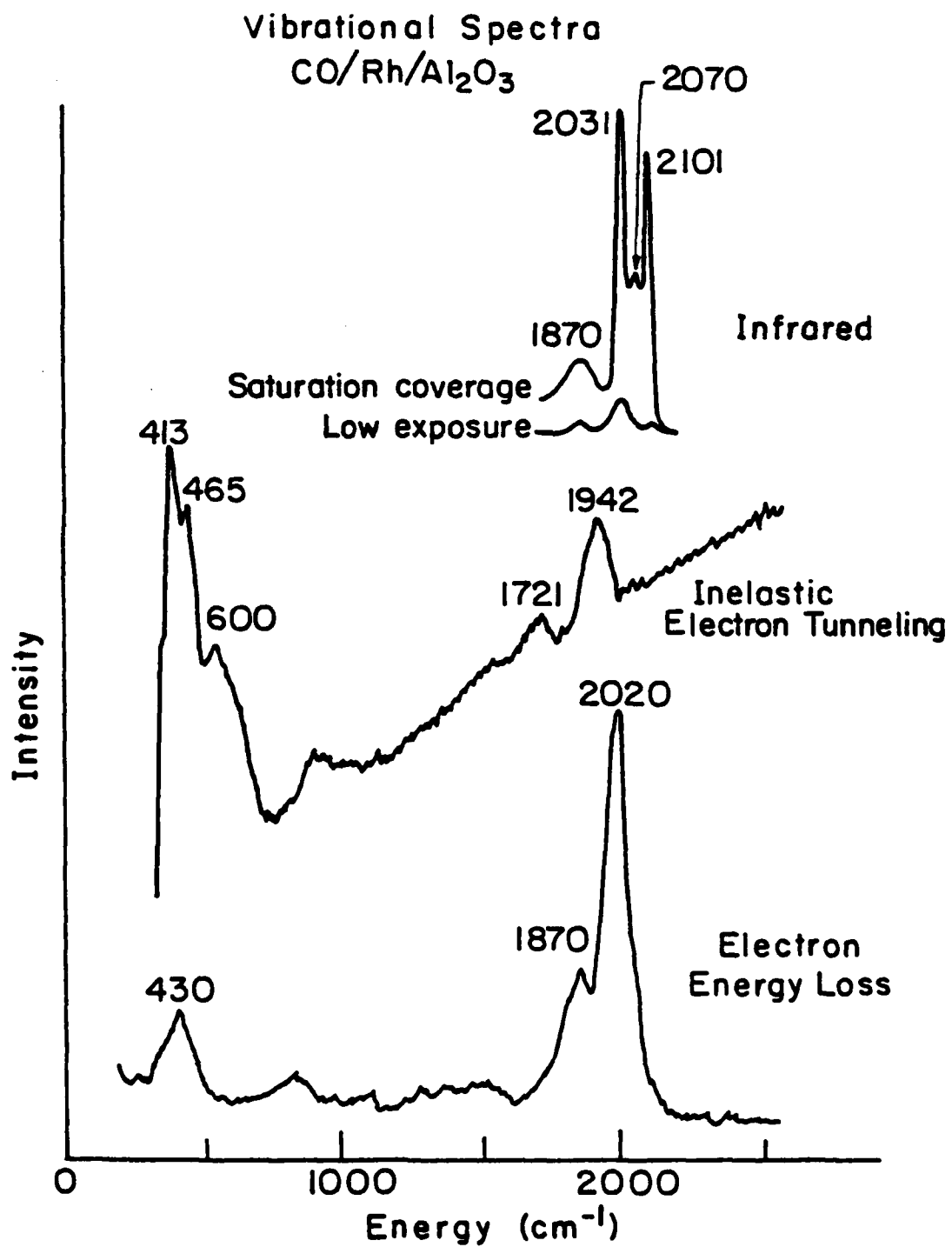


FIGURE 37



XBL802-4733



FIGURE 38

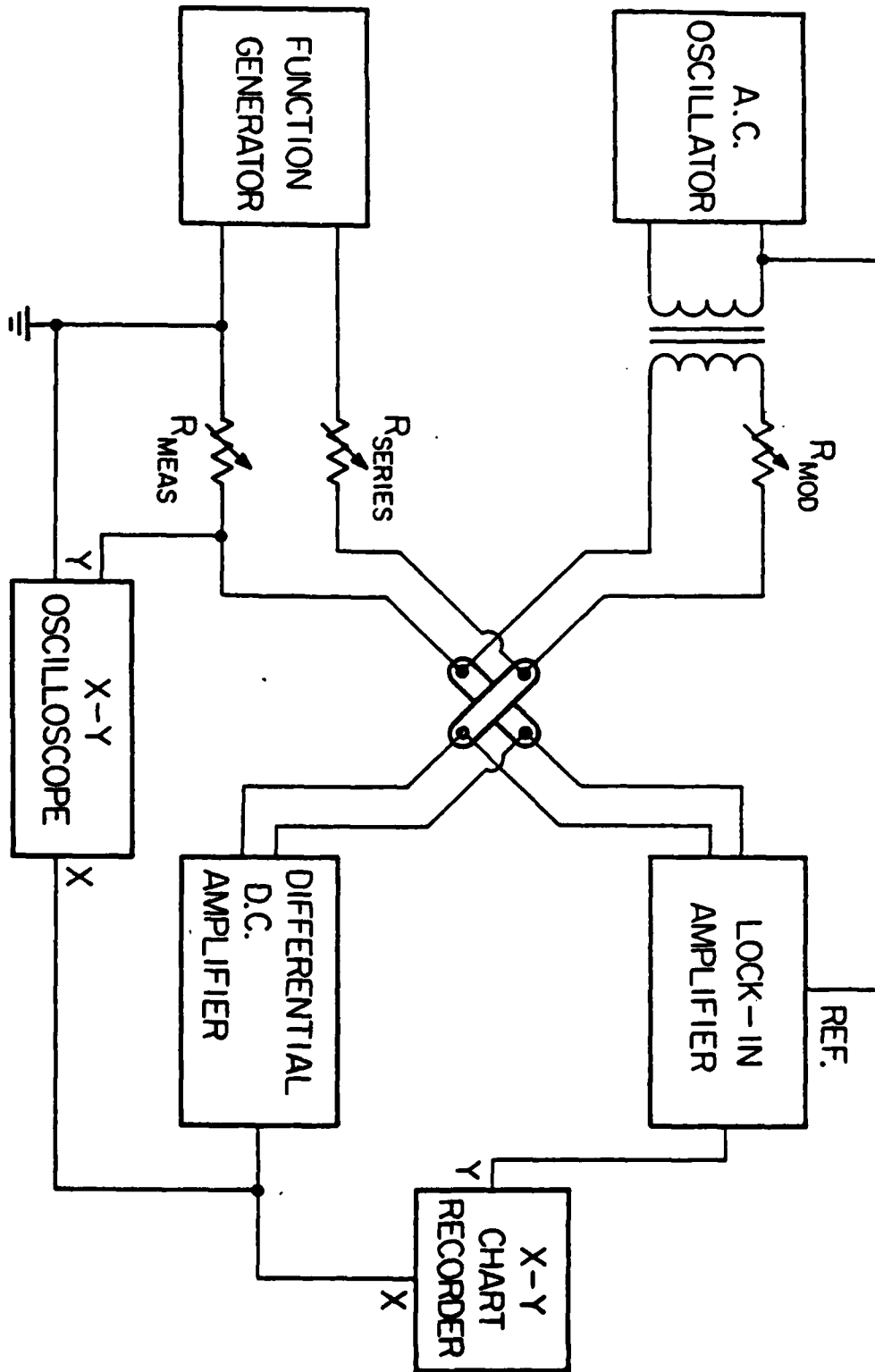


TABLE 1

## Resolution and Trace Times for Tunneling Spectra

Temperature	Modulation	Resolution	Trace Time				Peak Shift	Relative	Trace Time
		mV	cm <sup>-1</sup>	1 sec	3 sec	10 sec	mV	cm <sup>-1</sup>	(Same Signal:Noise)
4.2 K	2.0 mV	3.9	32	15 min	40 min	2.0 hr	0.7	6	1
4.2 K	1.0 mV	2.6	21	20 min	1.0 hr	3.0 hr	0.9	7	11
4.2 K	0.7 mV	2.1	17	25 min	1.2 hr	3.5 hr	1.0	8	46
1.0 K	2.0 mV	3.4	28	15 min	40 min	2.0 hr	0.7	6	1.1
1.0 K	1.0 mV	1.8	14	30 min	1.5 hr	5.0 hr	0.9	7	17
1.0 K	0.7 mV	1.3	10	40 min	2.0 hr	6.0 hr	1.0	8	65

**DATE**  
**ILME**